

CHARGE-BASED COMPACT MODEL OF GATE-ALL-AROUND FLOATING
GATE NANOWIRE WITH VARIABLE OXIDE THICKNESS FOR FLASH
MEMORY CELL

MUHAMMAD AFIQ NURUDIN BIN HAMZAH

UNIVERSITI TEKNOLOGI MALAYSIA

CHARGE-BASED COMPACT MODEL OF GATE-ALL-AROUND FLOATING
GATE NANOWIRE WITH VARIABLE OXIDE THICKNESS FOR FLASH
MEMORY CELL

MUHAMMAD AFIQ NURUDIN BIN HAMZAH

A thesis submitted in fulfilment of the
requirements for the award of the degree of
Doctor of Philosophy

Faculty of Electrical Engineering
Universiti Teknologi Malaysia

JUNE 2018

To my beloved family and friends.

ACKNOWLEDGEMENT

I would like to express my deepest appreciation to whom I owe a debt in completing this Phd work.

First, I would like to express my very great appreciation to my supervisor, Professor Dr. Razali Bin Ismail for such valuable advice and wonderful mentoring. Through his experience in man-management and enthusiasm, he paved the path for me in becoming a well-around academician and researcher. He tirelessly giving valuable advice and encouragement to become success in academia by rapidly and continually to publish academic work. He always quoted “*publish or perish*” has been a taboo and benchmark for me in pursuing success.

Secondly, I also thank to my co-supervisor, Dr. Nurul Ezaila Bt. Alias for all the technical support and advice that inevitably improved the quality of my work. Her endearing supervision has made me even more motivated in delivering positive and quality output for my research work.

My companions in the Computational Nanoelectronic Research lab for all the support in variety of ways. Special thanks to Lim Wei Hong, Fatimah Khairiah and Sakinah for sharing their ideas and giving significant contribution in improving my works. Not to forget Mr. Zulkifli, Maryati Morsin, Adila Syaidatul, Zuriana and Wei How for their support.

Million thanks to my family, especially to my parents, for all their understandings and emotional supports for giving me the encouragement to go forth in my career and life.

I would like to thank the Universiti Teknologi Malaysia (UTM) for the Zamalah Scholarship and it has been a privilege staying here. Last but not least, to the Ministry of Science, Technology and Industry (MOSTI) for providing funds for conference travels and publication charges.

ABSTRACT

Due to high gate electrostatic control and introduction of *punch* and *plug* process technology, the gate-all-around (GAA) transistor is very promising in, and apparently has been utilized for, flash memory applications. However, GAA Floating Gate (GAA-FG) memory cell still requires high programming voltage that may be susceptible to cell-to-cell interference. Scaling down the tunnel oxide can reduce the Program/Erase (P/E) voltage but degrades the data retention capability. By using Technology-Computer-Aided-Design (TCAD) tools, the concept of tunnel barrier engineering using Variable Oxide Thickness (VARIOT) of low- k /high- k stack is utilized in compensating the trade-off between P/E operation and retention characteristics. Four high- k dielectrics (Si_3N_4 , Al_2O_3 , HfO_2 and ZrO_2) that are commonly used in semiconductor process technology are examined with SiO_2 as its low- k dielectric. It is found that by using $\text{SiO}_2/\text{Al}_2\text{O}_3$ as the tunnel layer, both the P/E and retention characteristics of GAA-FG can be compensated. About 30% improvement in memory window than conventional SiO_2 is obtained and only 1% of charge-loss is predicted after 10 years of applying gate stress of -3.6V. Compact model of GAA-FG is initiated by developing a continuous explicit core model of GAA transistor (GAA Nanowire MOSFET (GAANWFET) and Junctionless Nanowire Transistor (JNT)). The validity of the theory and compact model is identified based on sophisticated numerical TCAD simulator for under 10% maximum error of surface potential. It is revealed that with the inclusion of partial-depletion conduction, the accuracy of the core model for GAANWFET is improved by more than 50% in the subthreshold region with doping-geometry ratio can be as high as about 0.86. As for JNT, despite the model being accurate for doping-geometry ratio upto 0.6, it is also independent of fitting parameters that may vary under different terminal biases or doping-geometry cases. The compact model of GAA-FG is completed by incorporating Charge Balance Model (CBM) into GAA transistor core model where good agreement is obtained with TCAD simulation and published experimental work. The CBM gives better accuracy than the conventional capacitive coupling approach under subthreshold region with approximately 10% error of floating gate potential. Therefore, the proposed compact model can be used to assist experimental work in extracting experimental data.

ABSTRAK

Oleh kerana kawalan elektrostatik get yang tinggi dan pengenalan kepada teknologi proses *tebuk* dan *plak*, transistor get-silinder-menyeluruh (GAA) sangat meyakinkan, dan telah digunakan dalam aplikasi memori *flash*. Walaubagaimanapun, GAA get terapung (GAA-FG) masih memerlukan voltan program yang tinggi yang mungkin terdedah kepada gangguan *cell-to-cell*. Pengecilan-skala terowong oksida dapat mengurangkan voltan program/padam (P/E) tetapi menyebabkan kemerosotan kepada daya-engekalan datanya. Dengan menggunakan perisian rekabentuk-berbantuan-teknologi-komputer (TCAD), konsep Kejuruteraan Terowong Penghadang Oksida Boleh-ubah (VARIOT) *k*-rendah/*k*-tinggi telah digunakan dalam konteks mengimbangi kurang-lebih antara operasi program/padam dan daya-engekalan data. Empat dielektrik *k*-tinggi (Si_3N_4 , Al_2O_3 , HfO_2 , ZrO_2) yang kebiasaannya terdapat dalam industri semikonduktor dianalisa dengan SiO_2 sebagai dielektrik *k*-rendah. Hasil simulasi menunjukkan gabungan $\text{SiO}_2/\text{Al}_2\text{O}_3$ sebagai lapisan terowong GAA-FG dapat mengimbangi kurang-lebih antara operasi program/padam dan daya-engekalan data. Sebanyak 30% peningkatan jendela memori berbanding SiO_2 dan hanya 1% kehilangan cas dijangkakan selapas 10 tahun dikenakan voltan-get setinggi -3.6V. Model kompak bagi GAA-FG dimulai dengan penghasilan model eksplisit berterusan untuk transistor GAA (GAANWFET dan JNT). Kesahihan antara teori dan model kompak dipastikan berdasarkan perisian simulasi TCAD bagi ralat maksimum beza-upaya permukaan sebanyak 10%. Hasil menunjukkan, dengan mengambil kira kesan konduksi separa-habis dapat meningkatkan ketepatan model-teras GAANWFET sebanyak lebih daripada 50% dalam kawasan sub-ambang untuk nisbah dopan-geometri sehingga 0.86. Bagi JNT pula, disamping model kompaknya tepat untuk nisbah dopan-geometri sehingga 0.6, ia juga tidak bergantung kepada parameter-cubaan yang mungkin berubah-ubah bagi voltan-terminal atau nisbah dopan-geometri yang berbeza. Model kompak GAA-FG disempurnakan hasil gabungan model pengimbang-cas (CBM) dan model kompak transistor GAA yang mana ketepatannya teruji baik dengan simulasi TCAD dan hasil eksperimen yang sudah diterbitkan. CBM memberikan ketepatan yang lebih baik berbanding kaedah kapasitif-gandingan konvensional pada bahagian sub-ambang dengan ralat beza-upaya get-terapung sebanyak 10%. Oleh itu, model kompak yang dihasilkan dapat digunakan untuk membantu kerja-kerja eksperimen bagi mengekstrak nilai parameter.

TABLE OF CONTENTS

CHAPTER	TITLE	PAGE
	DECLARATION	ii
	DEDICATION	iii
	ACKNOWLEDGEMENT	iv
	ABSTRACT	v
	ABSTRAK	vi
	TABLE OF CONTENTS	vii
	LIST OF TABLES	xi
	LIST OF FIGURES	xii
	LIST OF ABBREVIATIONS	xxii
	LIST OF SYMBOLS	xxv
	LIST OF APPENDICES	xxviii
1	INTRODUCTION	1
	1.1 Research Background	1
	1.2 Flash Memory Scaling Challenges and Motivation	3
	1.3 Problem Statements	8
	1.4 Research Objectives	11
	1.5 Research Scopes	12
	1.6 Research Contribution	12
	1.7 Thesis Organization	13
2	LITERATURE REVIEW	15
	2.1 Introduction	15
	2.2 Gate-All-Around Floating Gate (GAA-FG) Structures	15
	2.2.1 Planar GAA-FG Cell	16
	2.2.2 Vertical Channel GAA-FG cell	18

	2.2.2.1	Conventional-Floating Gate/Stacked-Surrounding Gate Transistor (C-FG/S-SGT)	18
	2.2.2.2	Dual Control Gate-Surrounding Floating Gate (DC-SF)	19
	2.2.2.3	Separated-Sidewall Control Gate (S-SCG)	20
	2.2.2.4	Sidewall Control Pillar (SCP)	22
2.3		Barrier Engineering Concept	23
	2.3.1	Crested Barrier	24
	2.3.2	VARIABLE Oxide Thickness (VARIOT)	27
	2.3.3	Crested Barrier versus VARIOT	30
2.4		Device Modeling	31
	2.4.1	Overview of GAANWFET Core Models	35
	2.4.2	Overview of Junctionless Nanowire Transistor (JNT) Core Models	44
	2.4.3	Explicit Solution to Core Model	51
	2.4.4	Floating Gate Potential Models	57
2.5		Summary	63
3		RESEARCH METHODOLOGY	64
	3.1	Introduction	64
	3.2	Research Activities	65
	3.3	Device Optimization and Characterization Approach	67
	3.4	Device Compact Modeling Approach	71
	3.5	Summary	73
4		GAA-FG WITH VARIOT TUNNEL LAYER DESIGN	75
	4.1	Introduction	75
	4.2	Parameter Optimization of Asymmetric VARIOT	75
	4.3	GAA-FG Simulation	83
	4.3.1	Validation Work of GAA-FG Memory Cell	83
	4.3.2	Device Performances of GAA-FG Cell Incorporating VARIOT Tunnel Layer	91
	4.4	Summary	96

5	CHARGE-BASED COMPACT MODELING OF GAA-FG	98
5.1	Introduction	98
5.2	Charge-Based Compact Model of GAANWFET	99
5.2.1	Implicit Continuous Charge-Based Model	100
5.2.2	Explicit Solution of Unified Charge Control Model (UCCM)	104
5.2.3	Current-Voltage (I-V), Charge-Voltage (Q-V) and Capacitance-Voltage (C-V) Characteristics	109
5.2.4	Partial-Depletion Conduction of GAAN-WFET	116
5.3	Charge-Based Compact Model of Junctionless Nanowire Transistor (JNT)	124
5.3.1	Implicit Continuous Charge-Based Model	125
5.3.2	Explicit Solution of Unified Charge Control Model (UCCM)	129
5.3.3	Current-Voltage (I-V), Charge-Voltage (Q-V) and Capacitance-Voltage (C-V) Characteristics	133
5.4	Floating Gate Potential Model of GAA-FG Memory Cell	141
5.5	Summary	147
6	CONCLUSION AND RECOMMENDATION	149
6.1	Introduction	149
6.2	Summary and Conclusion	149
6.2.1	TCAD simulation on optimization of VARIOT tunnel layer	149
6.2.2	TCAD simulation on GAA-FG performances using VARIOT tunnel layer	150
6.2.3	Charge-based compact model of GAAN-WFET	150
6.2.4	Charge-based compact model of JNT	151
6.2.5	Charge-based compact model GAA-FG memory cell	152
6.3	Future Works	153

REFERENCES

157

Appendices A – C

172 – 192

LIST OF TABLES

TABLE NO.	TITLE	PAGE
2.1	Common MOSFET models available in circuit simulators.	32
2.2	GAANWFET core models.	43
2.3	Development of JNT core models.	50
3.1	Flash memory operational constraints.	69
4.1	Parameters for different dielectric materials used in simulation.	76
4.2	Optimized parameters and extracted F-N coefficients for device characterization purpose.	82
4.3	Parameters used in simulation work and experimental GAA-FG cell in Lee <i>et al.</i> , (2013).	85
4.4	VARIOT physical thickness and EOT used in simulation.	91
A.1	Parameters and data for SiO ₂ /Si ₃ N ₄ extracted from TCAD simulation.	172
A.2	Parameters and data for SiO ₂ /Al ₂ O ₃ extracted from TCAD simulation.	174
A.3	Parameters and data for SiO ₂ /HfO ₂ extracted from TCAD simulation.	176
A.4	Parameters and data for SiO ₂ /ZrO ₂ extracted from TCAD simulation.	178

LIST OF FIGURES

FIGURE NO.	TITLE	PAGE
1.1	The memory device based on Complementary Metal-Oxide-Semiconductor (CMOS) technology divided into two categories, which are volatile and non-volatile.	1
1.2	(a) Number of storage capacity exponentially increase throughout the years with storage application devices is the highest. (Source from Forward Insight). (b) Memory revenue on some of the companies manufacturing various memory devices and the top five companies consolidation in memory industry, majorly dominated by companies that sold flash memory (source from Micron 2014 Winter Analyst Conference).	3
1.3	Summarized the downscaling issues in term of performance related to the gate stack of the conventional wraparound FG cell in NAND flash memory.	4
1.4	Scaling limitation of 2-D NAND flash. (a) Increments in cell-to-cell interference of a victim cell across BL, WL and diagonal FGs and (b) decrements in number of electron in floating gate.	5
1.5	Roadmap from top semiconductor foundries for scaling 2-D and 3-D NAND flash architectures (source from ICinsight, 2014).	6
1.6	(a) Comparison of relative bit cost of 3-D architecture NAND flash between the stacking of conventional 2-D planar NAND and Bit-Cost Scalable (BiCS) NAND technology as the number of layer increases. (b) BiCS fabrication method.	7
1.7	(a) Comparison of threshold voltage shift after program with control gate voltage (V_{cg}) and after bulk erase between C-FG, S-SCG and SCP 3-D NAND cells. (b) Trade-off between P/E scalability and retention characteristics for different tunnel oxide thickness.	9

2.1	(a) Fabrication steps for GAA-FG memory cell and (b) the cross-section of the device consists of control gate (CG), floating gate (FG), SiO ₂ tunnel oxide, SiO ₂ IPD layer and poly-Si channel.	16
2.2	Electric field of (a) GAA-SONOS charge trapping and (b) GAA-FG during program at 10 ⁻⁶ and 10 ⁻³ s.	17
2.3	(a) Fabrication process steps for IMFT 3-D NAND flash C-FG memory cell and (b) the cross-section of its memory cell consists of control gate (CG), floating gate (FG), IPD oxide layer, tunnel oxide and poly-Si channel.	19
2.4	(a) Fabrication process steps for SK Hynix 3-D NAND flash DC-SF memory cell and (b) the cross-section of the memory cell showing the poly-Si floating gate (FG) and its two poly-Si control gates (CGs) with IPD oxide layer separating between them.	20
2.5	(a) Fabrication process steps for SK Hynix 3-D NAND flash with S-SCG memory cell and (b) the cross-section of the memory cell showing the two SCGs act as electrical S/D layer.	21
2.6	(a) Fabrication process steps for SK Hynix 3-D NAND flash with SCP memory cell and (b) the cross-section of the memory cell showing the poly-Si pillar and its dimension of length, L _{scp} and width, W _{scp} .	22
2.7	Shows the conduction band diagram of (a) typical uniform height barrier, (b) and (c) are the ideal form of symmetric and asymmetric crested barrier respectively. (d) and (e) are the actual form of symmetric and asymmetric crested barrier respectively. Parameter e , V , U , U' , d and d' are the electron charge, applied bias, low-k energy barrier, high-k energy barrier, low-k layer thickness, and high-k layer thickness.	24
2.8	Conduction band diagram between (a) typical uniform barrier, (b) symmetric crested barrier and (c) asymmetric crested barrier during retention (no applied bias V) and after applied bias V . U is the low-k barrier height and U' is the high-k barrier height.	25
2.9	The current density (dashed lines) and the gate recharging time (lines) of the crested barriers and single-layer barrier with various physical thickness. The notations of the plot (a)-(e) are in accordance to Figure 2.7.	26

2.10	Comparison of J_G against applied bias for crested and single-layer barriers with same EOT of 5nm. Y_3O_2 , Si_3N_4 and ZrO_2 have been used as the outer layer of crested barriers being Al_2O_3 and SiO_2 as the middle layer.	27
2.11	Schematic shows the stacking of (a) symmetric VARIOT and (b) asymmetric VARIOT with their respective band diagram at flat-band condition.	28
2.12	Comparison of the conduction band diagram for (a) asymmetric and (b) symmetric VARIOT structures with the single-layer SiO_2 barrier during retention and applied bias V .	28
2.13	(a) Comparison of $J_G - V$ characteristics between VARIOT and single layer SiO_2 . (b) Summarizes the advantages of VARIOT (straight line) having steeper slope than SiO_2 (dotted line) for EOT=5nm.	29
2.14	Comparison of (a) $J_G - V_{FG}$ characteristics for various combinations of crested barrier and VARIOT with EOT=5nm. (b) Sketch of the conduction band diagram of symmetric VARIOT showing electron injection in both elastic and inelastic limits.	31
2.15	Definition of compact modeling with its analytical approaches and solution.	34
2.16	Schematic cross-section of GAANWFET and its related variables.	36
2.17	Comparison of drain current between model and TCAD simulation (Circles) for $R = 10$ nm from intrinsic to high body concentration upto $1 \times 10^{19} \text{cm}^{-3}$.	40
2.18	(a) Normalized potential for intrinsic to body concentration of $3 \times 10^{18} \text{cm}^{-3}$. (b) Comparison of drain current between model in Zhang <i>et. al.</i> , (2009) (Red lines) and Liu <i>et. al.</i> , (2008) (Black lines) with TCAD simulation (Squares) for $R = 10$ nm.	42
2.19	Comparison of schematic structure between JNT device to the conventional inversion-mode (IM) transistor. JNT has identical dopant concentration in the body to that of the S/D regions ($n^+/n^+/n^+$).	44
2.20	Transfer characteristics and its operation regimes of (a) Junctionless Nanowire Transistor and (b) conventional inversion-mode GAANWFET.	45

2.21	Comparison of CV characteristics at gate terminal between compact model developed by Oana <i>et al.</i> , (2014) with TCAD Atlas simulation results for (a) various high-dopant concentration and (b) small-radii.	49
2.22	Schematic of CCCM floating gate cell, where C_{cg} , C_{ox} , C_d , and C_s are the capacitances between FG and CG, channel, drain and source respectively.	58
2.23	I-V curves of reference (R) and floating gate devices (F) for $V_d = 0.1V$ (R1 and F1) and $V_d = 0.6V$ (R2 and F2). S is the subthreshold slope of the FG cell and S_0 is the subthreshold slope of the reference cell.	60
2.24	Schematic of CBM FG memory cell, consists of control gate capacitance C_{cg} , MOS transistor equivalent to the memory cell, and voltage-controlled voltage source (VCVS) of floating gate, V_{fg} .	61
3.1	Research methodology flowchart of GAA-FG memory cell with VARIOT tunnel layer and GAA devices compact modeling.	66
3.2	Flowchart for device simulation work.	67
3.3	Parameters involved in simulation of GAA-FG cell using asymmetric VARIOT tunnel oxide with its comparative study.	71
3.4	Flowchart for device modeling work.	72
4.1	Metal-Oxide-Semiconductor (MOS) capacitor structure with low-k/high-k stack as its gate oxide.	76
4.2	JV characteristics of SiO_2/Si_3N_4 for EOT=4nm. The horizontal dashed-lines are the imposed constraints during program, read-disturb and retention. The red dashed-lines just to show the boundaries of electron tunneling mechanism for $T_{ox}=3nm$ depending of V_{tr} and V_{fn} .	77
4.3	$V_g - T_{ox}$ plot of program constraint for (a) SiO_2/Si_3N_4 (b) SiO_2/Al_2O_3 (c) SiO_2/HfO_2 and (d) SiO_2/ZrO_2 .	79
4.4	$V_g - T_{ox}$ plot of read-disturb and retention constraints for (a) SiO_2/Si_3N_4 (b) SiO_2/Al_2O_3 (c) SiO_2/HfO_2 and (d) SiO_2/ZrO_2 . The upper plot ($V_g > 0$) is after imposing the read-disturb constraint at $J_g = 7 \times 10^{-11} A/cm^2$ and the lower plot ($V_g \leq 0$) is after imposing the retention constraint at $J_g = 2 \times 10^{-16} A/cm^2$. The symbols are consistent with legend in Figure 4.3.	80

- 4.5 Optimized gate voltage for each EOT of all asymmetric VARIOTs due to (a) retention constraint of $>|-1.5V|$ and (b) a more restrictive read-disturb constraint of $>3.6V$. 81
- 4.6 (a) The cross-section of experimental GAA-FG with triangular nanowire. (b) The cross-section of GAA-FG structure showing silicon nanowire channel and source/drain region with its electrode, and poly-Si FG being surrounded by SiO_2 . 84
- 4.7 Comparison of transfer characteristics between 3-D simulation with experimental data by Lee *et al.*, (2013) for drain bias of 0.1V and 1.0V. Device simulation with (line) and without (dashed-line) definition of interface traps near the conduction are also shown. 86
- 4.8 Comparison of P/E characteristics between simulation and experimental data in Lee *et al.*, (2013) for a given P/E voltages of 10/-8V up to 10ms. P/E characteristics of GAA-FG cell with T_{ox} scaling limit of 6nm SiO_2 to indicate fast charging. 87
- 4.9 Electric field distribution along the radial direction of GAA-FG cell in (a) simulation and (b) extracted experimental result in Lee *et al.*, (2013). 88
- 4.10 Comparison of retention characteristics between GAA-FG cell of 8nm and 11nm SiO_2 with experimental data (black) in Lee *et al.*, (2013) after a P/E cycle for P/E voltages of 10/-8V and P/E time of 5/2ms. The lines are the 10 years extrapolation results of threshold voltage using Power's law. 90
- 4.11 (a) Fabrication process of C-FG cell with an additional deposition of high-k dielectric before low-k and poly-Si channel were form. (b) Schematic diagram of GAA-FG cell with asymmetric VARIOT as tunnel oxide layer. T_{ox} and T_H are the thickness for low-k and high-k dielectric materials. 91
- 4.12 JV characteristics for various low-k/high-k tunnel layer. All stacks have physical thickness of 11nm. The 6nm and 8nm SiO_2 layer are the control device to indicate high program current and retention characteristics. Steeper slope and gate current density are achieved with decreasing of EOT. 92

4.13	(a) C-V curves for various low-k/high-k tunnel layer. (b) Electric field profile of GAA-FG cells across the gate stack. SiO ₂ /Al ₂ O ₃ stack yield the utmost surface field at Si/SiO ₂ interface.	93
4.14	Comparison of P/E characteristics of GAA-FG cell using VARIOT tunnel layer with GAA-FG of 6nm SiO ₂ . indicates faster P/E operation but higher voltage is required for erase operation.	94
4.15	Retention characteristics of GAA-FG with VARIOT tunnel layer of (a) SiO ₂ /Si ₃ N ₄ (b) SiO ₂ /Al ₂ O ₃ , (c) SiO ₂ /HfO ₂ and (d) SiO ₂ /ZrO ₂ under gate stress of -3.6/3.6V. Data retention for GAA-FG of 8nm SiO ₂ is plotted to benchmark 20% charge-loss under similar gate stress.	96
4.16	Performance comparison of GAA-FG incorporating VARIOT tunnel layer with experimental results in Lee <i>et al.</i> , (2013).	97
5.1	Schematic diagram for n-channel GAANWFETs with cylindrical coordinate system. The diagram also shows the distribution of interface trap densities, D_{it} and fixed oxide charges, Q_f .	100
5.2	Comparison of mobile charge density between explicit expression of Equation (5.16) with iterative/implicit solution of Equation (5.13).	105
5.3	Comparison of Q_m against V_g curves at $V_d = 0V$ between explicit model (5.19) and implicit model from intrinsic ($N_A = 1.45 \times 10^{10} \text{cm}^{-3}$) to higher doping concentration of $1 \times 10^{19} \text{cm}^{-3}$.	107
5.4	Comparison of Q_m against V_g curves at $V_d = 0V$ between explicit model (5.19) and implicit UCCM for a wide range of R in (a) intrinsic and (b) higher doping concentration ($N_A = 1 \times 10^{19} \text{cm}^{-3}$).	107
5.5	Comparison of Q_m against V_g curves at $V_d = 0.05V$, between explicit model (5.19) and implicit UCCM for various range of Q_f in (a) intrinsic and (b) higher doping concentration ($N_A = 1 \times 10^{19} \text{cm}^{-3}$).	108
5.6	Comparison of Q_m against V_g curves at $V_d = 0.05V$, between explicit model (5.19) and implicit UCCM for various range of D_{it} in (a) intrinsic and (b) higher doping concentration ($N_A = 1 \times 10^{19} \text{cm}^{-3}$).	108

- 5.7 Assuming zero trap state density ($Q_f = 0$, and $\eta = 1$), (a) shows the $I_{ds} - V_g$ curves of GAANWFET from intrinsic to high doping concentration and (b) the $I_{ds} - V_d$ curves with wide range of operating gate voltage are verified with 3D device simulation. 110
- 5.8 Given Q_m from (5.19), comparison of $I_{ds} - V_g$ for (a) fixed oxide charges and (b) interface trap densities against numerical simulation are in good agreement. 110
- 5.9 Comparison between explicit models in Cheralathan *et al.*, (2011) and (5.19) with implicit UCCM solution for $N_A = 1 \times 10^{17} \text{cm}^{-3}$ and $N_A = 1 \times 10^{19} \text{cm}^{-3}$. (a) Shows the Q_m against V_g curves and (b) I_{ds} against V_g at $V_d = 1.0\text{V}$. 111
- 5.10 Comparison between analytical model with numerical TCAD simulation of (a) normalized transconductance and (b) conductance for $V_d=0.05\text{V}$ and 1.0V . Terminal charges of GAANWFET (c) against V_g and (d) against V_d for $N_A = 3 \times 10^{18} \text{cm}^{-3}$. The parameters are consistent for all figures. 113
- 5.11 Comparison of intrinsic capacitances across (a)-(c) gate voltage and (b) drain voltage between analytical models with numerical TCAD simulation results for heavily doped body of $N_A=3 \times 10^{18} \text{cm}^{-3}$. Analytical models fairly predict the transition region for a given accurate explicit solution of the mobile charge expression. Symbols are consistent for both plots. 115
- 5.12 Surface potential due to dopant carrier in partial-depletion conduction of Equation (5.36) and full-depletion conduction of Equation (5.37) for (a) FD-GAANWFET and (b) PD-GAANWFET. The partial-depletion conduction is shown to be affected by (c) dopant concentration and (d) radius. 118
- 5.13 Surface and center potentials of GAANWFET with $N_A=1 \times 10^{19} \text{cm}^{-3}$ computed using unified function of N for (a) $N=4$ and (b) $N=12$. Optimum value of N is obtained by comparing with TCAD simulation. 120
- 5.14 Optimum value of N extracted by comparison with TCAD simulation. The proposed model for N (red-line) fit well with extracted data (dot-symbol). Inset shows the error of analytical model with referenced to TCAD simulation results for varying $qN_A R^2 / 4\epsilon_{Si}$ ratio. 120

5.15	Surface potential model with and without the inclusion of partial-depletion conduction compared to TCAD simulation for (a) different dopant concentration and (b) its percentage error; for (c) different radii and (d) its percentage error.	121
5.16	Comparison of (a) mobile charge density and (b) transfer characteristics for various dopant concentration.	122
5.17	Transfer characteristics with various radii for dopant concentration of (a) $N_A=1\times 10^{16}\text{cm}^{-3}$ and (b) $N_A=1\times 10^{18}\text{cm}^{-3}$. Output characteristics for dopant concentration of (c) $N_A=1\times 10^{16}\text{cm}^{-3}$ and (d) $N_A=1\times 10^{18}\text{cm}^{-3}$ respectively.	123
5.18	Schematic diagram for JNT with cylindrical coordinate system. The diagram also shows the interface trap densities, D_{it} and the fixed oxide charges, Q_f are assume to be uniformly distributed along the channel.	125
5.19	Assessment of UCCM model for all operating regions of JNT at $V_d = V_s = 0V$. The red vertical lines denote the threshold and flat-band voltages to indicate the boudaries of operating region from full-depletion (FD), partial-depletion (PD) and accumulation (ACC).	129
5.20	Mobile charge density for depletion (Q_{DP}) and complementary (Q_C) parts at $V_d=0V$. The total mobile charge Q_m agreed well with numerical simulation by making Q_C as complementary charge to Q_{DP} .	131
5.21	(a) Comparison of surface potential computed using analytical model with referenced to TCAD simulation and (b) its error.	132
5.22	Comparison of mobile charge density between proposed model with Duarte <i>et al.</i> , (2012) that was solved using iterative method for various (a) dopant concentration and (b) radius.	133
5.23	Transfer characteristics of JNT for various (a) high dopant concentration and (b) radius compared to numerical TCAD simulation.	135
5.24	Output characteristics for $R=10\text{nm}$ at dopant concentration of (a) $N_D=5\times 10^{18}\text{cm}^{-3}$ and (b) $N_D=1\times 10^{19}\text{cm}^{-3}$.	136
5.25	Comparison of (a) transconductance, (b) conductance and terminal charges against (c) gate voltage and (d) drain voltage.	139

- 5.26 Comparison of all the capacitances (i.e.:- self-capacitances and transcapacitances) across (a)-(c) gate voltage and (d) drain voltage between analytical models with numerical TCAD simulation results for dopant concentration of $N_D=1 \times 10^{19} \text{ cm}^{-3}$. Analytical models fairly predict the partial depletion region. Symbol and parameter are consistent for all plots. 140
- 5.27 Cross-section of a symmetrical GAA-FG. R is the radius, L_g is the gate length while T_{ox} and T_{IPD} are the tunnel oxide and IPD oxide thicknesses respectively. C_{cg} is the FG-CG capacitance, C_{ox} is the tunnel oxide capacitance and the intrinsic capacitances with respect to floating gate terminal are denoted as C_{gd} and C_{gs} . The channel charge, Q_{ch} is equal to the total charge across the gate stack that sum as $Q_{fg} + C_{cg} (V_{cg} - V_{fg})$. 142
- 5.28 Floating gate potential for various (a) drain voltage and (b) predefined Q_{fg} . For CCCM, fixed capacitive ratios of $\alpha_{cg}=0.64$ and $\alpha_d=0.18$ are re-used from CBM to fit with TCAD simulation as well as total capacitance given as $C_{tot}=C_{cg}+C_{ox}+C_d+C_s$, with C_d and C_s are extracted from TCAD simulation as 0.038fF and 0.12fF respectively. 143
- 5.29 Transfer characteristics of GAA-FG for various (a) drain voltage and (b) predefined Q_{fg} . 143
- 5.30 (a) Comparison of proposed model with experimental data. All parameters remain the same as in Table 4.2 except for Q_f and interface traps parameter η that are treated as fitting parameter. (b) Comparison of floating gate potential between proposed model and CCCM approach with referenced to TCAD simulation. Fixed capacitive ratio of $\alpha_{cg}=0.73$ and $\alpha_d=0.14$ from CBM is re-used in CCCM approach. 145
- 5.31 (a) Control gate coupling (α_{cg}) and (b) drain coupling (α_d) ratios of GAA-FG for $Q_{fg}=0$ and varying V_{cg} and V_d using V_{fg} calculated from the charge balance model. 146
- 5.32 Comparison of GCR at $V_d=0V$ for VARIOT tunnel layer with referenced to conventional 11nm SiO_2 tunnel layer of GAA-FG fabricated in Lee *et al.*, (2013). 147

6.1	An array of 3-D FG-NAND that consists of four FG cell and two select transistors. Capacitances show the coupling between selected FG cell with neighbouring-FG (NFG), control gate and neighbouring control gate (NCG).	154
6.2	(a) Block diagram of read path-circuit and its (b) sense amplifier.	156
A.1	$J_g - V_g$ characteristics of $\text{SiO}_2/\text{Si}_3\text{N}_4$ for EOT (a) 4nm (b) 5nm (c) 6nm (d) 7nm and (e) 8nm.	173
A.2	$J_g - V_g$ characteristics of $\text{SiO}_2/\text{Al}_2\text{O}_3$ for EOT (a) 4nm (b) 5nm (c) 6nm (d) 7nm and (e) 8nm.	175
A.3	$J_g - V_g$ characteristics of $\text{SiO}_2/\text{HfO}_2$ for EOT (a) 4nm (b) 5nm (c) 6nm (d) 7nm and (e) 8nm.	177
A.4	$J_g - V_g$ characteristics of $\text{SiO}_2/\text{ZrO}_2$ for EOT (a) 4nm (b) 5nm (c) 6nm (d) 7nm and (e) 8nm.	179
A.5	(a) JV characteristics for the optimized parameters of all asymmetric VARIOTs conducted. F-N plot of all asymmetric VARIOTs conducted for (b) programming and (c) erase operations.	180

LIST OF ABBREVIATIONS

ACM	-	Advanced Compact MOSFET
ALCVD	-	Atomic Layer Chemical Vapor Deposition
AT	-	Above Threshold
BiCS	-	Bit-Cost Scalable
BIOS	-	Basic Input Output Storage
BT	-	Below Threshold
BSIM	-	Berkeley Short-Channel IGFET Model
CBM	-	Charge Balance Model
CCCM	-	Capacitive Coupling Coefficient Model
C-FG	-	Conventional-Floating Gate
CD-ROM	-	Compact-Disk Read-Only-Memory
CLM	-	Channel Length Modulation
CMOS	-	Complementary Metal-Oxide-Semiconductor
CT	-	Charge Trapping
CTCI	-	Cell-to-Cell Interference
DC-SF	-	Dual-Control Gate Surrounding-Floating Gate
DIBL	-	Drain Induced Barrier Lowering
DRAM	-	Dynamic Random Access Memory
DVD-ROM	-	Digital-Versatile-Disc Read-Only-Memory
DQT	-	Direct Quantum Tunneling
EEPROM	-	Electrically Erasable Programmable Read-Only-Memory
EKV	-	Enz-Krummenacher-Vittoz
EPRM	-	Erasable Programmable Read-Only-Memory
EOT	-	Effective Oxide Thickness
ETOX	-	EPRM Tunnel Oxide
FG	-	Floating Gate
FD	-	Fully-Depleted
F-N	-	Fowler-Nordheim
GAA	-	Gate-All-Around
GAANWFET	-	Gate-All-Around Nanowire Field-Effect-Transistor

GCA	-	Gradual Channel Approximation
GCR	-	Gate Capacitance Ratio
HDD	-	Hard-Disk Drive
HiSIM	-	Hiroshima-University STARC IGFET Model
IGFET	-	Insulated Gate Field-Effect-Transistor
IPD	-	Inter-Poly Dielectric
ITRS	-	International Technology Roadmap for Semiconductor
JNT	-	Junctionless Nanowire Transistor
LPCVD	-	Low-Pressure Chemical Vapour Deposition
MLC	-	Multi-Level Cell
MM11	-	MOS Model 11 Philips
MOS	-	Metal-Oxide-Semiconductor
MOSFET	-	Metal-Oxide-Semiconductor Field-Effect Transistor
MOS-C	-	Metal-Oxide-Semiconductor Capacitor
MONOS	-	Metal-Oxide-Nitride-Oxide-Silicon
NVM	-	Non-Volatile Memory
PD	-	Partially-Depleted
PROM	-	Programmable Read-Only-Memory
PSP	-	Philips's MM11 and Surface Potential
RAM	-	Random-Access-Memory
ROM	-	Read-Only-Memory
SCP	-	Sidewall Control Pillar
SOI	-	Silicon-on-Insulator
SONOS	-	Silicon-Oxide-Nitride-Oxide-Silicon
SPICE	-	Simulation Program with Integrated Circuit Emphasis
SRAM	-	Static Random-Access-Memory
SS	-	Subthreshold Slope
SSD	-	Solid-State Drive
STARC	-	Semiconductor Technology Academic Research Center
TBE	-	Tunnel Barrier Engineering
TCAD	-	Technology Computer Aided Design
TCAT	-	Terabit Cell Array Transistor
TLC	-	Tri-Level Cell
UCCM	-	Unified Charge Control Model
USB	-	Universal Serial Bus
VARIOT	-	Variable Oxide Thickness

VCVS	-	Voltage-Controlled Voltage-Source
XiP	-	Execute-in-Place

LIST OF SYMBOLS

A_{FN}	-	F-N coefficient
A_W	-	cross-section area
A_{gate}	-	gate area
B_{FN}	-	F-N coefficient
C_{ox}	-	gate oxide capacitance
C_{IPD}	-	inter-poly oxide capacitance
C_{eff}	-	effective gate capacitance
C_{gg}	-	gate-gate capacitance
C_{gs}	-	gate-source capacitance
C_{gd}	-	gate-drain capacitance
C_{dd}	-	drain-drain capacitance
C_{dg}	-	drain-gate capacitance
C_{ds}	-	drain-source capacitance
C_{ss}	-	source-source capacitance
C_{sg}	-	source-gate capacitance
C_{sd}	-	source-drain capacitance
D_{it}	-	interface trap charge density
E	-	electric field
E_s	-	surface field
E_G	-	band gap
g_m	-	transconductance
g_d	-	conductance
m^*	-	effective mass
m_0	-	electron effective mass
N_A	-	acceptor doping
N_D	-	donor doping
n_i	-	intrinsic concentration
n_0	-	center concentration
t_{ret}	-	retention time
T_{ox}	-	silicon dioxide thickness

T_{hk}	-	high-k dielectric thickness
T_{tun}	-	tunnel oxide thickness
T_{FG}	-	floating gate thickness
I_{ds}	-	drain current
I_{dC}	-	complementary drain current
I_{dDP}	-	depletion drain current
J_g	-	gate current density
L_g	-	gate length
Q_{fg}	-	floating gate charge
Q_m	-	mobile charge density
Q_C	-	complementary mobile charge density
Q_{DP}	-	depletion mobile charge density
Q_{eff}	-	effective charge density
Q_{dep}	-	depletion charge density
Q_{ch}	-	channel charge
Q_{bulk}	-	bulk charge
Q_g	-	gate charge
Q_d	-	drain charge
Q_s	-	source charge
Q_f	-	fixed oxide charge
Q_{sc}	-	semiconductor charge
R	-	radius
V_{fn}	-	F-N voltage
V_{tr}	-	transition voltage
V_g	-	gate voltage
V_{cg}	-	control gate voltage
V_{fg}	-	floating gate potential
V_{FB}	-	flat-band voltage
V_d	-	drain voltage
V_s	-	source voltage
V_{prog}	-	program voltage
V_{ers}	-	erase voltage
$V_{read-dist}$	-	read disturb voltage
V_{ret}	-	retention voltage
V_T	-	threshold voltage
α_{cg}	-	gate capacitance ratio

α_d	-	drain capacitance ratio
α_s	-	source capacitance ratio
μ	-	effective mobility
ΔV_T	-	threshold shift
$\Delta\varphi$	-	workfunction difference
ϕ	-	potential distribution
ϕ_c	-	correction potential
ϕ_s	-	surface potential
ϕ_0	-	center potential
ϕ_{dep}	-	full-depletion potential
ϕ_{pert}	-	perturbation potential
ϕ_f	-	fermi potential
ϕ_t	-	thermal voltage
ϕ_B	-	barrier height
ϕ_{ox}	-	silicon dioxide barrier height
ϕ_{hk}	-	high-k barrier height
ϵ_0	-	vacuum permittivity
ϵ_{Si}	-	silicon permittivity
ϵ_{ox}	-	silicon dioxide permittivity
ϵ_{hk}	-	high-k permittivity
ϵ_r	-	dielectric constant
η	-	interface trap parameter
χ	-	electron affinity
γ	-	body coefficient

LIST OF APPENDICES

APPENDIX	TITLE	PAGE
A	Parameter Optimization of Asymmetric VARIOT	172
B	Derivation of Charge-Based Compact Model	181
C	Publication List	192

CHAPTER 1

INTRODUCTION

1.1 Research Background

Moore's law has led to the advancement of high-speed logic computing, increasing number of electronic consumer and information technology that urge for higher data storage capability. Memory as one of the constituent of electronic devices has been continuously developed for providing massive data storage and high-speed applications. It is used in many consumer electronic appliances where encoded data is to be stored and retained as digital information inside a memory device. Memory can be divided into two main categories, which are volatile and non-volatile memory (NVM) as shown in Figure 1.1.

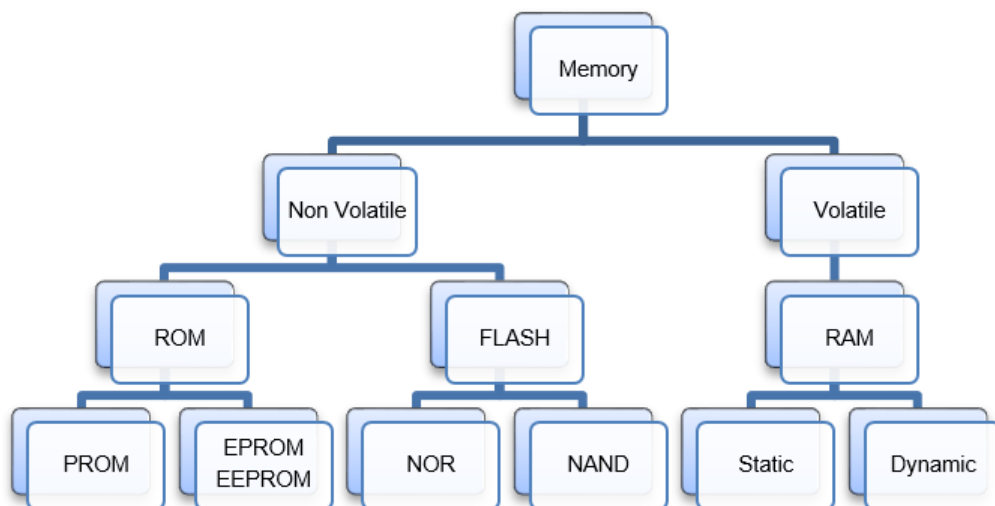


Figure 1.1: The memory device based on Complementary Metal-Oxide-Semiconductor (CMOS) technology divided into two categories, which are volatile and non-volatile.

Volatile memory is a form of memory that loses data when the power is off. It is

also referred as Random-Access-Memory (RAM) with very fast read and erase time. Dynamic-RAM (DRAM) and Static-RAM (SRAM) are the commonly known volatile memory. Whereas, non-volatile memory is a form of memory that preserves the data even when the power is off. It is also known as Read-Only-Memory (ROM). NVM can retain massive amount of data but at lower write and read speed than the volatile memory. Mask ROM, Programmable ROM (PROM), Erasable PROM (EPROM), Electrically Erasable-Programmable ROM (EEPROM) and Flash Memory are the types of NVM. All of these memory devices are based on metal-oxide-semiconductor (MOS) technology. There are also other technologies that have been used to store data. Optical devices such as compact-disk ROM (CD-ROM), digital-versatile-disc RAM (DVD-RAM) and ferroelectric technology such as the well-known hard-disk drive (HDD) are employed as dominant secondary memory, in which all of these are commonly used to store digital information.

EEPROM provides with a practical usage of data storage device where the Program/Erase (P/E) operation is performed by applying electric field to the transistor cell's terminals. Furthermore, it also provides with byte-wise random access capability that made EEPROM a key figure for data storage application and to perform execute-in-place (XiP) operation. However, each of EEPROM's transistor cell or memory cell is form by two-transistor (2T), which made the device highly expensive and consumes very large circuit layout for massive storage application [1]. Flash memory is another type of NVM that had been developed from EEPROM. Instead of having 2T per cell, flash memory only consists of one-transistor (1T) per cell and has been a revolution in directing the course of memory industry into sub-20nm half-pitch scaling [2]. Because of its 1T per cell structure, the relative bit cost can be greatly reduced compared to EEPROM and it has been vastly used in many today's electronic appliances ever since. This has been proven based on a statistical study as shown in Figure 1.2(a) that the memory storage capacity exponentially increased within almost a decade (2007-2014). The emergence of mobile smart phone and solid state drive (SSD) have rapidly increased the storage capacity from 10,000 million GB to 70,000 million GB in a short span of four years (2010-2014). This has led to over 20% market share increment from the consolidation of some of the top semiconductor manufacturers such as Samsung, Micron, Hynix, Toshiba and SanDisk in which all of these companies hugely contribute to the manufacturing of mobile smart phone and SSD (refer Figure 1.2(b)).

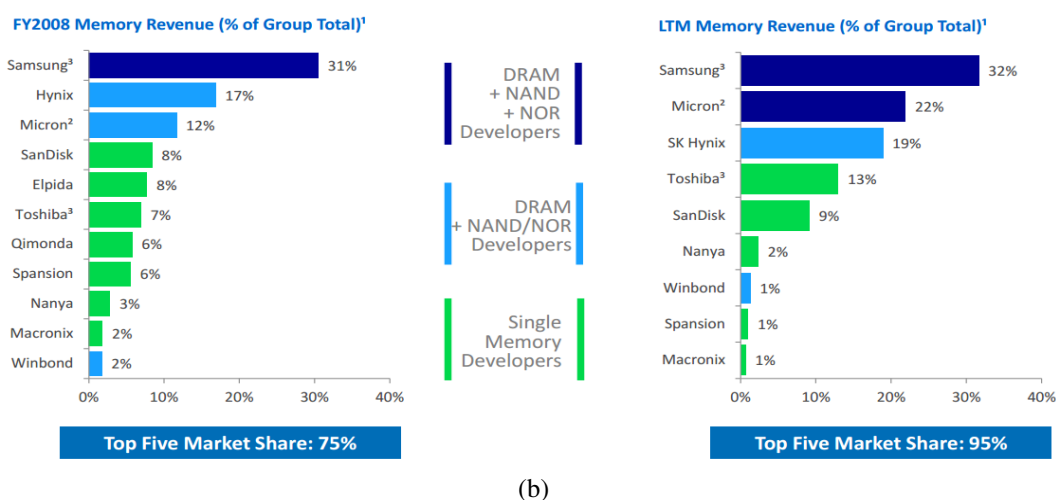
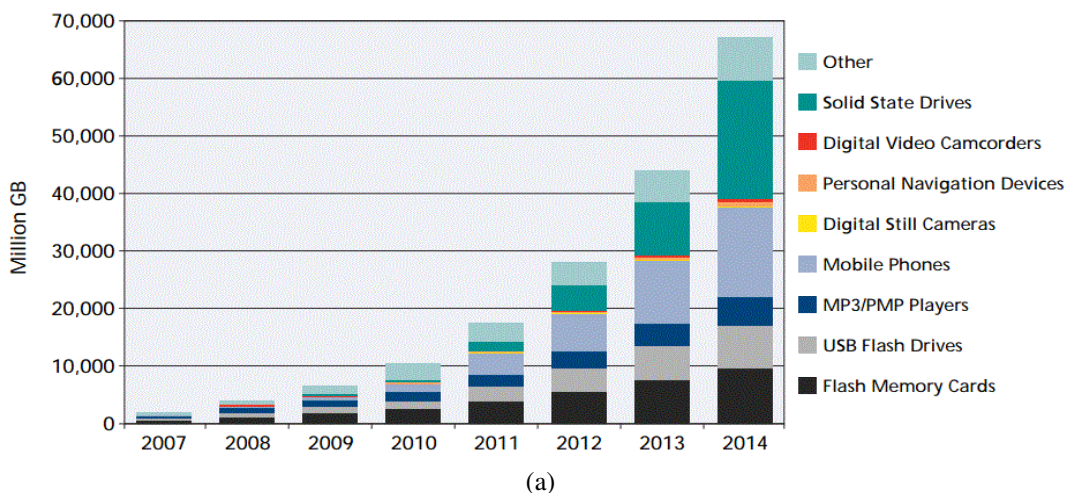


Figure 1.2: (a) Number of storage capacity exponentially increase throughout the years with storage application devices is the highest. (Source from Forward Insight). (b) Memory revenue on some of the companies manufacturing various memory devices and the top five companies consolidation in memory industry, majorly dominated by companies that sold flash memory (source from Micron 2014 Winter Analyst Conference).

1.2 Flash Memory Scaling Challenges and Motivation

For more than two decades, floating gate (FG) memory cell has been commonly utilized in many flash memory devices. To increase the storage capacity of flash memory and to continue the exponential growth of the industry, scaling of FG cell is inevitable. However, downscaling of the FG cell has reached its bottleneck as the cell encounter physical limitations that degrade its memory performances. Figure 1.3 summarizes the issues for each component of the gate stack of the FG cell (i.e.: poly-Si FG, poly-Si control gate, inter-poly dielectric and tunnel oxide) in understanding the interrelation and the trade-off in their performances. These issues becoming more

and more severe due to oppression in gate capacitance ratio (GCR) which was caused by capacitive coupling between adjacent cells that subsequently decreases the gate electrostatic control. In order to improve the gate control while scaling its P/E voltages, the floating gate need to be wrap-around by the control gate and the thickness of dielectric layers need to be reduced but at the expense of its reliability (i.e.: retention and endurance) and add stronger coupling effect with neighboring cells. Therefore, it has been very challenging to sustain the $GCR \geq 0.6$ as well as to scale its P/E voltages while maintains its high-speed operation, especially for sub-20nm half-pitch.

Poly-Si Control Gate

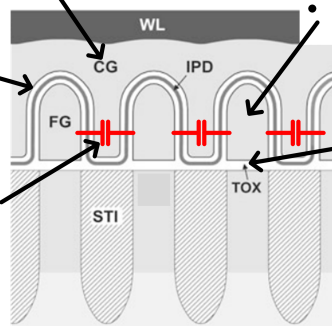
- Scalable P/E voltages require thinner IPD and/or tunnel oxide layers.
- Cannot accommodate wrap-around CG for sub-20nm half-pitch decreases the GCR

IPD Oxide Layer

- Thickness limited at 10nm in order to maintain $GCR \geq 0.6$.
- Downscaling increases CTCL effects.
- Thin IPD layer increases gate leakage during programming.

Cell-to-cell Interference (CTCI)

- Due to $GCR < 0.6$.
- Causes Program, Erase and Read disturb.
- Unstable bit-states of a cell.
- Reduces the programming speed.



Poly-Si Floating Gate

- Vertical Scaling limited at 7nm thick.
- Very few number of stored charges.
- Electron charges went ballistic from FG into CG.
- Towering FG increases CTCL effects

Tunnel Oxide

- Thickness limited at 5-6nm.
- Severe wearing effects for thickness $< 8\text{nm}$.
- Stress-induced leakage current (SILC).
- Severe charge-loss due to thin oxide layer.
- Edge field enhancement reduces gate electrostatic control.

Figure 1.3: Summarized the downscaling issues in term of performance related to the gate stack of the conventional wraparound FG cell in NAND flash memory.

As shown in Figure 1.3, each component of the gate stack contributes to the reduction of GCR that affect the P/E performances of the FG cell. One of the major concerns of GCR reduction has been the scaling of its dielectric layers. An ideal dielectric material in FG cell is to provide fast P/E operation as well as scalable P/E voltages and to avoid from any electron leakage during program and retention, thus, granting the non-volatile capability. International Technology Roadmap for Semiconductor (ITRS) predicted that both the thickness of inter-poly dielectric (IPD) and tunnel oxide layers are restrained at 10nm and 6-7nm respectively while maintained the $4F^2$ cell size. This signifies the end of conventional symmetric scaling of $2F \times 2F$ at 20nm half-pitch given the floating gate distance along the same word-line (WL) only provides enough space for the IPD layer [2]. Continue scaling down the IPD thickness means the distance between FG cells in the same WL is

getting cramped; as a result, the GCR will be reduced prior to stronger coupling with neighboring floating gates. Moreover, to maintain the $4F^2$ cell size also implies that the distance between FG cells across the bit-line (BL) must be reduced creating fringing capacitance not only across the BL but also with diagonal FG cells as well [3]. This has added the variability to the threshold voltage of the selected cell and led to abnormal cell-to-cell interference (CTCI) effects. Such effects are the unstable bit states of FG cell that caused disturb during P/E and read operations, and also reducing its speed [4, 5]. Therefore, with continuous downscaling the CTCI effects are exponentially increased towards the 20nm half-pitch as shown in Figure 1.4(a). Other issue in scaling has been the floating gate itself as the electron charges continue to decrease with downscaling as shown in Figure 1.4(b). The figure also depicts the amount of critical electron charges before severe threshold voltage disturbance start to occur leading to unstable bit-state. In the case of tunnel oxide scaling, the high-field stress during P/E operation has caused severe wearing of the dielectric layer due to the introduction of negative trapped charges [6]. With frequent P/E cycles the negative trapped charges will steadily piled up and increases the threshold voltage, which subsequently degrades its dc (e.g.: Sub-threshold slope (SS), threshold voltage variation) and transient performances (i.e.: retention) [7].

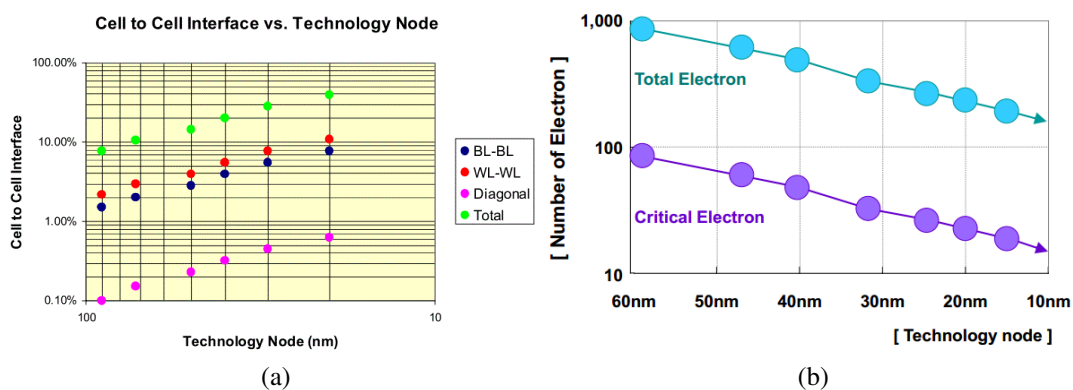


Figure 1.4: Scaling limitation of 2-D NAND flash. (a) Increments in cell-to-cell interference of a victim cell across BL, WL and diagonal FGs [4] and (b) decrements in number of electron in floating gate.

Due to restraints and limitations in FG cell dielectric thickness, it is difficult to effectively scale the 2-D NAND flash memory. Figure 1.5 shows the scaling projection from some of the top flash memory manufacturers. In mid-2012, SanDisk defies the symmetric $4F^2$ scaling of the FG cell and introduced the asymmetric $19\text{nm} \times 26\text{nm}$ per cell to provide enough space for IPD layer and retain the wrap-around poly-Si control gate technology. As flash memory continue to scale, it will only be a matter of time

before it reaches the horizon and stops at 10-12nm half-pitch due to the statistical limits of charge stored inside the floating gate for beyond 10nm node. Therefore, an indefinite increase of memory storage may not be possible through device scaling. Instead, it has been increased by stacking multiple layers of planar NAND array to form three-dimensional (3-D) NAND flash architecture [8]. However, stacking the conventional planar structure to form 3-D NAND flash requires additional photolithography process depending on the number of layers, which is technically challenging and can be very expensive.

NAND Flash Process Roadmaps (for Volume Production)

	2011	2012	2013	2014	2015	2016	2017	
IM Flash		20nm	16nm		10-12nm	Gen 1	Gen 2	2D 3D
Samsung		21nm	24L	16nm	32L		10-12nm	2D 3D
						Gen 3 (48L)		
SK Hynix		20nm	16nm		10-12nm	Gen 1	Gen 2	2D 3D
Toshiba/SanDisk		19nm	15nm		10-12nm	Gen 1	Gen 2	2D 3D

Figure 1.5: Roadmap from top semiconductor foundries for scaling 2-D and 3-D NAND flash architectures (source from ICinsight, 2014).

The emergence of Bit-Cost Scalable (BiCS) technology using ‘*punch*’ and ‘*plug*’ process offers cheaper and higher number of vertical stack than conventional planar NAND flash memory [9]. Figure 1.6(a) depicts cheaper relative bit-cost for higher number of stack compared to 3-D stacked planar NAND. The ‘*punch*’ and ‘*plug*’ terms refer to the fabrication method that *punch* through multi-layer of electrodes and insulators with single lithography process before *plug* holes with channel films to form Gate-All-Around (GAA) transistor (refer Figure 1.6(b)). There are various types of 3-D NAND flash being manufactured nowadays, in which all of these architectures implemented the GAA structure as their cell transistor and employed either floating gate (FG) or charge-trapping (CT) as their memory element. Samsung and Toshiba have adopted the CT cell for their 3-D NAND namely the Terabit Cell Array Transistor (TCAT) and pipe-shaped Bit-Cost Scalable (p-BiCS) respectively [10, 11]. However, 3-D CT NANDs are known to be susceptible to charge-spreading in the nitride-trapping layer that led to poor distribution of cell-state and degrades the retention characteristics [12]. Therefore, some of the top semiconductor companies, such as Hynix and Intel/Micron Flash Technologies (IMFT) preferred FG cell for their 3-D

NAND flash [13, 14]. The reasons for maintaining floating gate as the memory element in 3-D vertical NAND architectures are due to:

1. The 3-D stacked architecture with surrounding FG can circumvent the lateral charge spreading that occurs in the charge trapping layer along the BL.
2. The poly-Si FG provides high energy barrier (3.15eV) from electron tunneling during retention.

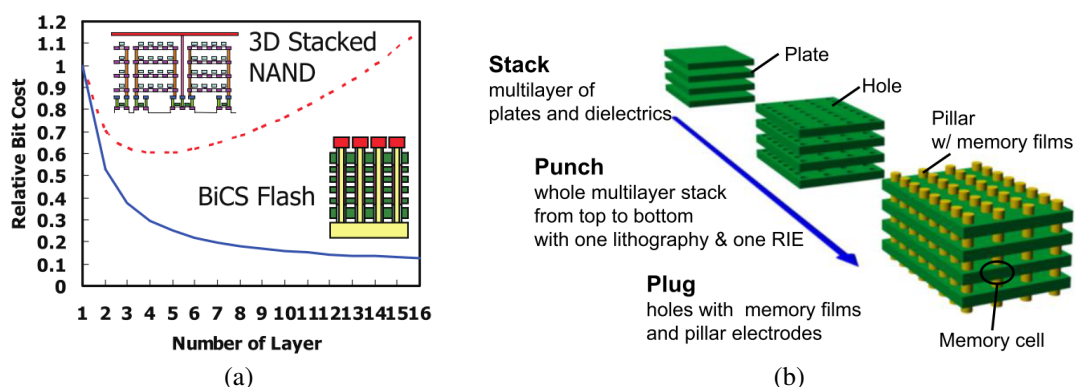


Figure 1.6: (a) Comparison of relative bit cost of 3-D architecture NAND flash between the stacking of conventional 2-D planar NAND and Bit-Cost Scalable (BiCS) NAND technology as the number of layer increases. (b) BiCS fabrication method [9].

SK Hynix has been actively developing their 3-D FG NAND flash. Various form of 3-D FG cells was proposed such as the Dual-Control Gate Surrounding-Floating Gate (DC-SF), the Separated-Sidewall Control Gate (S-SCG) and the Sidewall Control Pillar (SCP). The most notable has been the SCP cell due to its capability of suppressing the interference effects, cell disturbances, fast P/E operation and accommodate downscaling to 20nm half-pitch. However, in early 2016, it was IMFT that caught the attention of computer consumers by announcing their first generation 3-D vertical NAND [14]. The 3-D NAND cell is based on Conventional-Floating Gate (C-FG) structure that uses the double poly-Si technology and conventional P/E schemes. Due to its large physical cell size compared to the 20nm NAND, better performance can be achieved. The wide memory window of approximately $>10V$ is obtained indicating a greater number of electron stored in the floating gate. This gives a good indication for Multi-Level Cell (MLC) and Tri-Level Cell (TLC) applications, where 256Gbit (MLC)/384Gbit (TLC) data per die is expected to be stored in 32-layers vertical stack. The GAA structure also plays an important role in giving strong electrostatic gate control to improve the coupling

effects by aggressively reducing the total interference effects and threshold voltage distribution in planar 20nm 2-D NAND by ~80% and ~50% respectively [14]. Larger gate width/length ratio also added to its gate control capability to compensate the low mobility of polysilicon channel and increases the string on-current. In addition, it is reported that the IMFT 3-D cell with 32-layer vertical stack has the highest bit density of 1.52Gb/mm² compared to Samsung CT cell of 1.01 Gb/mm².

1.3 Problem Statements

Although the 3-D FG cell possesses relevant number of reliability advantages and high bit density compared to the 3-D CT cell, it also co-exists with cell-to-cell interference causes by poor coupling at the floating gate and become more severe when it comes to 3-D stacked architecture that led to higher programming voltage than its CT counterpart [15]. As can be seen from Figure 1.7(a), C-FG cell requires higher program voltage to yield wide threshold shift compared to SCP and S-SCG cells. Applying high program voltage on a select cell can induce high-field at channel interface and speedup the programming time, but this may eventually cause over-programming to its neighboring cells. Thinning the tunnel oxide thickness can also boost the programming speed and provides scalable P/E voltages but increases the rate of electrons tunneling back into the channel during retention. Figure 1.7(b) depicts dramatic charge-loss in planar CT cell for tunnel oxide thickness below 4nm. As for the case of FG cell, the tunnel oxide can hardly be scaled below 6-7nm to prevent from severe charge loss [2]. Therefore, there has been a trade-off between scaling the tunnel oxide for scalable program voltage with data retention.

Nonetheless, given its conventional P/E schemes and less number of variability issues, the C-FG cell with GAA structure seems has been utilized as 3-D NAND flash memory [14]. In order to provide fast program operation and 10 years data retention, the tunnel dielectric layer must be scaled. A tunnel barrier engineering concept known as Variable Oxide Thickness (VARIOT) has been proposed through combinations of low-k/high-k stack to deal with the trade-off of P/E characteristics performance without severely jeopardizing the data retention capability [16, 17]. Govoreanu *et. al.*, (2003) have shown that by stacking the high-k material such as ZrO₂ on top of the low-k SiO₂ can increase the gate tunneling current while very low current is observed at low gate bias due to its thick physical thickness [16]. However, this method has yet to be utilized in 3-D FG cell leaving question marks to what combination of low-k/high-k that is suitable for boosting the P/E operation speed and retention characteristics.

Considering the characteristics of VARIOT that yield high electric field in its layer and thicker physical thickness than SiO_2 , it is expected that the performances of P/E and reliability of GAA-FG can be compensated.

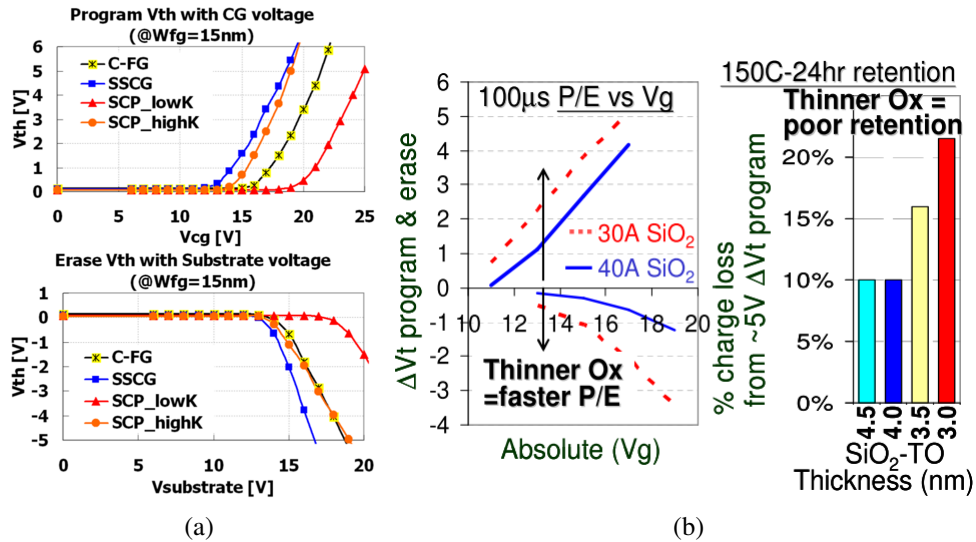


Figure 1.7: (a) Comparison of threshold voltage shift after program with control gate voltage (V_{cg}) and after bulk erase between C-FG, S-SCG and SCP 3-D NAND cells [18]. (b) Trade-off between P/E scalability and retention characteristics for different tunnel oxide thickness [19].

Computer Aided Design (CAD) tools have been vital for Integrated Circuit (IC) design. Circuit simulator is one of the CAD tools that have been widely used by designers in understanding circuit behavior and details of its operation. It allows quick evaluation of circuit performance without costly having to fabricate the integrated prototype. However, one should bear in mind that the accuracy of the results computed by the simulator depends on the quality of discrete device models. Thus, to acquire an accurate compact model, serve as the critical component for circuit designers in assessing the performance of mixed analog-digital circuit and play a crucial role in chip design productivity for semiconductor foundries.

A physics-based compact model is indispensable for device characterization, optimization and circuit simulation. A good compact model should meet several requirements, which are [20]:- the model is physically accurate, independent of fitting parameters, and also to ensure numerical convergence in Simulation Program with Integrated Circuit Emphasis (SPICE) simulator, the models must be described by an explicit and continuous expression over the entire operating regions [21]. Therefore, in order to accommodate experimental works for parameter extraction and to allow for

quick evaluation of circuitry or even discrete device performances, it is essential to develop a compact model for GAA-FG.

To model the electrical behaviour of GAA-FG cell, the GAA nanowire-FET (GAANWFET) core models must be comprehended. There are two types of GAANWFET which are the conventional GAANWFET and the most recent, junctionless-based GAANWFET or known as Junctionless Nanowire Transistor (JNT). Although there have been numerous works on compact modeling of GAANWFETs, especially for the conventional one, there are opportunities for further refinement. It can be described as follows;

For conventional GAANWFET:-

1. Several attempts are made to explicitly solve the arbitrary body-doped GAANWFET [22–24]. But the models are limited for dopant concentration up to $5 \times 10^{18} \text{ cm}^{-3}$ despite having empirical parameters being used [23] and neglected the importance of trap states along the channel for a realistic compact model. Furthermore, some of the models have also assumed zero flat-band voltage to fit the numerical TCAD simulation, which is physically unreasonable [24,25].
2. Another important feature in GAANWFET is the partial-depletion conduction in highly-doped condition. Most of the models developed for GAANWFET invoked the full-depletion approximation to simplify the nonlinearity of Poisson's equation so that it can be integrated across the channel length. Thus, the model is accurate only for fully-depleted device and limited to doping-geometry ratio up to 0.45 [23, 26–31] that can lead to misinterpretation of its subthreshold performance. An attempt to include the partial-depletion conduction and to extend the validity of doping-geometry ratio only results in poor accuracy to its low-doped body condition [32].

For Junctionless Nanowire Transistor (JNT):-

1. Most models reported for JNT are regional, and the current expressions are piecewise continuous, where additional smoothing functions that rely on fitting parameters are required to unify between regions [33–38]. In addition, there are other JNT models that are continuous but took an implicit form [39–41]. The implicit form solution requires iterative numerical method, which either

converges very slowly or does not converge due to imaginary value [42]. Therefore, a nonpiecewise continuous and explicit model is required for JNT.

2. Quasi-static terminal charges and capacitance are essential for ac and transient simulation. As far as this work is concerned, there are very few works that provide with analytical solution of terminal charges and capacitance for JNT [20, 43]. The developed solution for these parameters involves additional smoothing functions and rely on fitting parameters to fit the graph despite suffering in terms of accuracy as much as 16% [43]. While other, requires demanding derivation processes using partial derivative in solving the capacitance [20].

1.4 Research Objectives

The mutual target of this research is to design and enhance the performance of GAA-FG cell by implementing the concept of VARIOT and to develop its compact model using charge-based explicit expression. Based on the limitations and trade-offs in C-FG cell, also considering the performance expectation of VARIOT as the tunnel oxide layer, and the modeling issues in GAANWFET devices, the objectives are summarized as follow:

1. To optimize and determine a suitable VARIOT combination of low-k/high-k stack for GAA-FG cell in compensating the trade-off between P/E and retention characteristics.
2. Compact model of conventional GAANWFET:-
 - (a) To explicitly solve the mobile charge density for arbitrary body doping including the trap state effects.
 - (b) To analytically model the partial-depletion conduction.
3. Compact model of Junctionless Nanowire Transistor:-
 - (a) To explicitly solve the mobile charge density that is continuous for all operating regions.
 - (b) To obtain a continuous drain current, terminal charges and capacitance expressions.
4. To model the floating gate potential of GAA-FG.

1.5 Research Scopes

The scopes of this research will be confined as follows:

1. *GAA-FG Design*: The dimension and physical parameters of GAA-FG are based on experimental work performed by Lee *et al.*, (2013) [44]. Although the experimental data by Lee *et al.*, (2013) has used triangular nanowire as the channel, but in order to comply with vertical channel fabrication process the cylindrical channel has been used in this simulation work. In addition, the physical transport between triangular and cylindrical channels remain the same. Barrier Engineered of VARIOT tunnel oxide is limited to asymmetric combinations of low-k/high-k stack given the relevance for enhancing program operation and retention performances.
2. *Simulation Work*: Technological-Computer-Aided-Design (TCAD) simulation work is divided into two parts; parameters optimization and device simulation of GAA-FG. Based on MOS capacitor (MOS-C) structure and for a given flash memory constraint, extensive parameter optimization is conducted to obtain optimum parameter settings. Device simulation is performed to observe and analyze the transfer characteristics and transient memory performances of a discrete single-cell/transistor GAA-FG. Under this condition, the effects from neighbouring cell are omitted.
3. *Analytical Modeling*: Device compact modeling of GAA-FG, which involves obtaining the explicit expression of mobile charge densities for GAA nanowire-FET, and the floating gate potential model. The compact model is limited to the essence of core model, which are long-channel and constant mobility. Therefore, the compact model does not include advanced physical effects. The accuracy of the explicit expression is discussed based on the accuracy of previously published works and 3-D device simulation over practical terminal voltages.

1.6 Research Contribution

The significant contribution of this work can be highlighted as follow:-

1. *Optimization of VARIOT*: The optimization of VARIOT tunnel layer that consists of low-k/high-k stack is performed for various high-k materials in order to determine their optimum thickness and to extract its tunneling properties. The

extracted optimum thickness for various low-k/high-k stack can be used as a tunnel oxide layer in a memory cell devices. Given the nonlinear behaviour of tunnel barrier engineering, the tunneling properties of VARIOT such as Fowler-Nordheim (F-N) coefficients can be exploited by circuit designer in analyzing the P/E performances of a memory cell or even to analyze the effect of gate leakage in a MOSFET device that uses VARIOT as its gate oxide.

2. *GAA-FG with VARIOT tunnel layer*: Subsequent to the optimization of VARIOT, the optimized thickness of low-k/high-k stacks are employed as a tunnel layer in GAA-FG cell to improve its P/E characteristics as well as its data retention.
3. *Explicit and continuous compact model of GAA devices*: To the relevance of GAA-FG cell that adopted nanowire structure, the compact model of nanowire devices, which are the GAANWFET and the JNT are developed. In this study, due to the importance of highly-doped body of GAANWFET, the partial-depletion conduction is considered in improving the accuracy of the compact model. For the sake of avoiding numerical convergence and piecewise model, an explicit nonpiecewise and continuous compact model of JNT is developed.

1.7 Thesis Organization

Chapter 1 is the foundation of this research. A brief background on memory devices and its development throughout the years in highlighting on memory storage demand due to rapid technology advancement that prompt to the importance of flash memory. Then, scaling challenges and motivations of flash memory are highlighted that deduced the problem statements. Based on the problem statements, research objectives are identified. The scope of work has been clarified depending on the existing experimental and tools provided. Finally, the contributions of this work are highlighted.

Chapter 2 covers broad overview on 3-D NAND cell structures, where advantages and disadvantages from each structure are being highlighted. In conjunction with VARIOT tunnel layer, the concept of barrier engineering is discussed based on the types of dielectric stacking as well as its physical transport. Device modeling is briefly described before in-depth review on modeling approach of GAA nanowire-FET and floating gate potential modeling are discussed.

Chapter 3 discusses the research method of this work starting from general flow

and technical works that are being conducted in achieving the objectives. The tools that were used in this research are also highlighted. Furthermore, details on the approach taken in simulation work such as dielectric material, optimization method and physical models, and also compact modeling work such as model-flow and approximation techniques are presented in the form flowchart and discussed.

In Chapter 4, all the simulation results are presented, which includes optimization of VARIOT and characterization of GAA-FG in determining which VARIOT combination is the most prowess for its application as memory cell in providing fast P/E operation as well as 10 years data retention. As a consequent to simulation work of GAA-FG, Chapter 5 provides with a comprehensive explanation on analytical modeling with regards to all the issues highlighted in the research problem, until the compact model for GAA-FG is concluded.

Finally, Chapter 6 summarizes all the findings in this research and the contributions are highlighted. In addition, to ensure the continuation of this research and to add more promising contributions to compact model society, future works are provided.

REFERENCES

1. Bez, R., Camerlenghi, E., Modelli, A. and Visconti, A. Introduction to flash memory. *Proceedings of the IEEE*. 2003, vol. 91. 489–502.
2. International Technology Roadmap for Semiconductors (ITRS). *Process Integration, Devices and Structure*. Technical report. 2013.
3. Kim, Y. J., Kang, J. G., Lee, B., Cho, G.-S., Park, S.-K. and Choi, W. Y. Effects of abnormal cell-to-cell interference on p-type floating gate and control gate NAND flash memory. *Japanese Journal of Applied Physics*, 2014. 53(4S): 04ED12.
4. Prall, K. Scaling Non-Volatile Memory Below 30nm. *Non-Volatile Semiconductor Memory Workshop, 2007 22nd IEEE*. 2007. 5–10.
5. Van Houdt, J. Flash memory: a challenged memory technology. *2006 IEEE International Conference on Integrated Circuit Design and Technology, Proceedings*. 2006. 40–43.
6. Keeney, S. N. Dielectric Scaling Challenges and Approches In Floating Gate Non-Volatile Memories. *Proceedings of Electrochemical Society*. 2004. 151–158.
7. Ielmini, D. Overview of Modeling Approaches for Scaled Non Volatile Memories. *2009 International Conference on Simulation of Semiconductor Processes and Devices*. IEEE. 2009. 1–8.
8. Jung, S. M., Jang, J., Cho, W., Cho, H., Jeong, J., Chang, Y., Kim, J., Rah, Y., Son, Y., Park, J., Song, M. S., Kim, K. H., Lim, J. S. and Kim, K. Three dimensionally stacked NAND flash memory technology using stacking single crystal Si layers on ILD and TANOS structure for beyond 30nm node. *Technical Digest - International Electron Devices Meeting, IEDM*. 2006. 30–33.
9. Tanaka, H., Kido, M., Yahashi, K., Oomura, M., Katsumata, R., Kito, M., Fukuzumi, Y., Sato, M., Nagata, Y., Matsuoka, Y., Iwata, Y., Aochi, H. and Nitayama, A. Bit Cost Scalable Technology with Punch and Plug Process for Ultra High Density Flash Memory. *VLSI Technology, 2007 IEEE Symposium*

- on. 2007. 14–15.
10. Jang, J., Kim, H.-S., Cho, W., Cho, H., Kim, J., Shim, S. I., Jang, Y., Jeong, J.-H., Son, B.-K., Kim, D. W., Kim, K., Shim, J.-J., Lim, J. S., Kim, K.-H., Yi, S. Y., Lim, J.-Y., Chung, D., Moon, H.-C., Hwang, S., Lee, J.-W., Son, Y.-H., Chung, U.-I. and Lee, W.-S. Vertical Cell Array Using TCAT (Terabit Cell Array Transistor) Technology for Ultra High Density NAND Flash Memory. *2009 Symposium on VLSI Technology*. 2009. 14–15.
 11. Nitayama, A. and Aochi, H. Bit Cost Scalable (BiCS) flash technology for future ultra high density storage devices. *VLSI Technology Systems and Applications (VLSI-TSA), 2010 International Symposium on*. 2010. 130–131.
 12. Kang, C., Choi, J., Sim, J., Lee, C., Shin, Y., Park, J., Sel, J., Jeon, S., Park, Y. and Kim, K. Effects of Lateral Charge Spreading on the Reliability of TANOS (TaN/AIO/SiN/Oxide/Si) NAND Flash Memory. *Reliability physics symposium, 2007. proceedings. 45th annual. ieee international*. 2007. 167–170.
 13. Aritome, S., Whang, S., Lee, K., Shin, D., Kim, B., Kim, M., Bin, J., Han, J., Kim, S., Lee, B., Jung, Y., Cho, S., Shin, C., Yoo, H., Choi, S., Hong, K., Park, S. and Hong, S. A novel three-dimensional dual control-gate with surrounding floating-gate (DC-SF) NAND flash cell. *Solid-State Electronics*, 2013. 79(January): 166–171.
 14. Parat, K. and Dennison, C. A floating gate based 3D NAND technology with CMOS under array. *Technical Digest - International Electron Devices Meeting, IEDM*. 2016. 3.3.1–3.3.4.
 15. Micheloni, R. *3D Flash Memories*. 1st ed. Springer. 2016.
 16. Govoreanu, B., Blomme, P., Van Houdt, J. and De Meyer, K. Enhanced tunneling current effect for nonvolatile memory applications. *Japanese Journal of Applied Physics, Part 1: Regular Papers and Short Notes and Review Papers*, 2003. 42(4B): 2020–2024.
 17. Govoreanu, B., Blomme, P., Rosmeulen, M., Van Houdt, J. and De Meyer, K. VARIOT: a novel multilayer tunnel barrier concept for low-voltage nonvolatile memory devices. *Electron Device Letters, IEEE*, 2003. 24(2): 99–101.
 18. Seo, M. S., Choi, J. M., Park, S. K. and Endoh, T. Highly scalable 3-D vertical FG NAND cell arrays using the Sidewall Control Pillar (SCP). *2012 4th IEEE International Memory Workshop, IMW 2012*. 2012. 1–4.
 19. Gilmer, D. C., Goel, N., Park, H., Park, C., Verma, S., Bersuker, G.,

- Lysaght, P., Tseng, H.-H., Kirsch, P. D., Saraswat, K. C. and Jammy, R. Engineering the complete MANOS-type NVM stack for best in class retention performance. *2009 IEEE International Electron Devices Meeting (IEDM)*. IEEE. 2009. 1–4.
20. Jiang, C., Liang, R., Xu, J. and Alam, M. A. A Compact Quasi-Static Terminal Charge and Drain Current Model for Double-Gate Junctionless Transistors and Its Circuit Validation. *IEEE Transactions on Electron Devices*, 2017. 64(12): 4823–4830.
 21. Yu, B., Lu, H., Liu, M. and Taur, Y. Explicit Continuous Models for Double-Gate and Surrounding-Gate MOSFETs. *IEEE Transactions on Electron Devices*, 2007. 54(10): 2715–2722.
 22. He, J., Bian, W., Zhang, J., Feng, J., Zhang, X., Wu, W. and Chan, M. An explicit carrier-based compact model for nanowire surrounding-gate MOSFET simulation. *Molecular Simulation*, 2008. 34(1): 81–87.
 23. Cheralathan, M., Cerdeira, A. and Benjamin, I. Compact model for long-channel cylindrical surrounding-gate MOSFETs valid from low to high doping concentrations. *Solid-State Electronics*, 2011. 55(1): 13–18.
 24. Jin, X., Liu, X., Wu, M., Chuai, R., Lee, J.-H. and Lee, J.-H. A Continuous Current Model of Ultra-Thin Cylindrical Surrounding-Gate Inversion-Mode Si Nanowire nMOSFETs Considering a Wide Range of Body Doping Concentration. *Semiconductor Science and Technology*, 2013. 28(1): 15002.
 25. Jin, X.-S., Liu, X., Hyuck-In, K. and Jong-Ho, L. A Continuous Current Model of Accumulation Mode (Junctionless) Cylindrical Surrounding-Gate Nanowire MOSFETs. *Chin. Phys. Lett.*, 2013. 30(3): 038502.
 26. Liu, F., He, J., Zhang, L., Zhang, J., Hu, J., Ma, C. and Chan, M. A charge-based model for long-channel cylindrical surrounding-gate MOSFETs from intrinsic channel to heavily doped body. *IEEE Transactions on Electron Devices*, 2008. 55(8): 2187–2194.
 27. Liu, F., He, J., Zhang, L., Zhang, J., Hu, J., Zhang, X. and Chan, M. A complete charge based compact model for silicon nanowire FETs including doping and advanced physical effects. 2008. 157–160.
 28. Yu, Y. S., Cho, N., Hwang, S. W. and Ahn, D. Implicit Continuous Current-Voltage Model for Surrounding-Gate Metal-Oxide-Semiconductor Field-Effect Transistors Including Interface Traps. *IEEE Transactions on Electron Devices*, 2011. 58(8): 2520–2524.
 29. Liu, F., Zhang, J., He, F., Liu, F., Zhang, L. and Chan, M. A charge-based

- compact model for predicting the current-voltage and capacitance-voltage characteristics of heavily doped cylindrical surrounding-gate MOSFETs. *Solid-State Electronics*, 2009. 53(1): 49–53.
30. Cheng, Q., Hong, C., Kuo, J. B. and Chen, Y. A surface-field-based model for nanowire MOSFETs with spatial variations of doping profiles. *IEEE Transactions on Electron Devices*, 2014. 61(12): 4040–4046.
 31. Hong, C., Cheng, Q., Wang, P., Meng, W., Yang, L., Kuo, J. B. and Chen, Y. An Analytic Surface-Field-Based Quasi-Atomistic Model for Nanowire MOSFETs with Random Dopant Fluctuations. *IEEE Transactions on Electron Devices*, 2015. 62(12): 4179–4185.
 32. Zhang, L., Zhang, J., Liu, F., Chen, L., Xu, Y., Zhou, W. and He, F. An analytic channel potential based model for dynamic depletion surrounding-gate mosfets with arbitrary doping level. *2009 1st Asia Symposium on Quality Electronic Design*. 2009. 131–135.
 33. Gnani, E., Gnudi, A., Reggiani, S. and Bacarani, G. Theory of the Junctionless Nanowire FET. *IEEE Transactions on Electron Devices*, 2011. 58(9): 2903–2910.
 34. Sallese, J. M., Chevillon, N., Lallement, C., Iñiguez, B. and Prégaldiny, F. Charge-based modeling of junctionless double-gate field-effect transistors. *IEEE Transactions on Electron Devices*, 2011. 58(8): 2628–2637.
 35. Chen, Z., Xiao, Y., Tang, M., Xiong, Y., Huang, J., Li, J., Gu, X. and Zhou, Y. Surface-potential-based drain current model for long-channel junctionless double-gate MOSFETs. *IEEE Transactions on Electron Devices*, 2012. 59(12): 3292–3298.
 36. Lime, F., Santana, E. and Iñiguez, B. A simple compact model for long-channel junctionless Double Gate MOSFETs. *Solid-State Electronics*, 2013. 80: 28–32.
 37. Lime, F., Moldovan, O. and Iniguez, B. A compact explicit model for long-channel gate-all-around junctionless MOSFETs. Part I: DC characteristics. *IEEE Transactions on Electron Devices*, 2014. 61(9): 3036–3041.
 38. Hwang, B. W., Yang, J. W. and Lee, S. H. Explicit analytical current-voltage model for double-gate junctionless transistors. *IEEE Transactions on Electron Devices*, 2015. 62(1): 171–177.
 39. Duarte, J. P., Choi, S. J., Moon, D. I. and Choi, Y. K. A nonpiecewise model for long-channel junctionless cylindrical nanowire FETs. *IEEE Electron Device Letters*, 2012. 33(2): 155–157.

40. Hong, C., Yang, L., Cheng, Q., Han, T., Kuo, J. and Chen, Y. A Continuous Compact Model Incorporating Higher-Order Correction for Junctionless Nanowire Transistors with Arbitrary Doping Profiles. *IEEE Transactions on Nanotechnology*, 2016. PP(99): 1–8.
41. Hong, C., Yang, L., Cheng, Q., Han, T., Kuo, J. B. and Chen, Y. A Nonlinear Surface-Field Compact Model for Junctionless Nanowire MOSFETs. *2016 IEEE Workshop on Microelectronics and Electron Devices (WMED)*. 2016. 8–11.
42. Jandhyala, S. and Mahapatra, S. An Efficient Robust Algorithm for the Surface-Potential Calculation of Independent DG MOSFET. *IEEE Transactions on Electron Devices*, 2011. 58(6): 1663–1671.
43. Moldovan, O., Lime, F. and Iniguez, B. A Compact Explicit Model for Long-Channel Gate-All-Around Junctionless MOSFETs. Part II: Total Charges and Intrinsic Capacitance Characteristics. *IEEE Transactions on Electron Devices*, 2014. 61(9): 3042–3046.
44. Lee, K.-H., Lin, H.-c. and Huang, T.-y. Gate-All-Around Floating-Gate Memory Device with Triangular Poly-Si Nanowire Channels. *Japanese Journal of Applied Physics*, 2013. 14: 532–533.
45. Lee, K.-H., Tsai, J.-R., Chang, R.-D., Lin, H.-C. and Huang, T.-Y. Low-Voltage High-Speed Programming/Erasing Floating-Gate Memory Device with Gate-All-Around Polycrystalline Silicon Nanowire. *Applied Physics Letters*, 2013. 103: 153102.
46. Endoh, T., Kinoshita, K., Tanigami, T., Wada, Y., Sato, K., Yamada, K., Yokoyama, T., Takeuchi, N., Tanaka, K., Awaya, N., Sakiyama, K. and Masuoka, F. Novel Ultra High Density Flash Memory with A Stacked-Surrounding Gate Transistor (S-SGT) Structured Cell. *International Electron Devices Meeting, 2001. IEDM '01. Technical Digest*. 2001. 2.3.1–2.3.4.
47. Seo, M. S., Park, S. K. and Endoh, T. The 3-Dimensional Vertical FG NAND Flash Memory with a Novel Electrical S/D Technique Using the Extended Sidewall Control Gate (ECSG). *IEEE Transactions on Electron Devices*. 2011, vol. 58. 2966–2973.
48. Seo, M. S., Lee, B. H., Park, S. K. and Endoh, T. A Novel 3-D Vertical FG NAND Flash Memory Cell Arrays Using the Separated Sidewall Control Gate (S-SCG) for Highly Reliable MLC Operation. *2011 3rd IEEE International Memory Workshop, IMW 2011*. 2011. 1–4.
49. Whang, S., Lee, K., Shin, D., Kim, B., Kim, M., Bin, J., Han, J., Kim, S.,

- Lee, B., Jung, Y., Cho, S., Shin, C., Yoo, H., Choi, S., Hong, K., Aritome, S., Park, S. and Hong, S. A Novel Three-Dimensional Dual Control-Gate with Surrounding Floating-Gate (DC-SF) NAND Flash Cell for 1Tb File Storage Application. *Solid-State Electronics*, 2010, vol. 79. 166–171.
50. Aritome, S., Noh, Y., Yoo, H., Choi, E. S., Joo, H. S., Ahn, Y., Han, B., Chung, S., Shim, K., Lee, K., Kwak, S., Shin, S., Choi, I., Nam, S., Cho, G., Sheen, D., Pyi, S., Choi, J., Park, S., Kim, J., Lee, S., Hong, S., Park, S. and Kikkawa, T. Advanced DC-SF Cell Technology for 3-D NAND Flash. *IEEE Transactions on Electron Devices*, 2013. 60(4): 1327–1333.
51. Seo, M. S., Lee, B. H., Park, S. K. and Endoh, T. Novel Concept of the Three-Dimensional Vertical FG Nand Flash Memory using the Separated-Sidewall Control Gate. *IEEE Transactions on Electron Devices*, 2012. 59(8): 2078–2084.
52. Likharev, K. K. Layered tunnel barriers for nonvolatile memory devices. *Applied Physics Letters*, 1998. 73(15): 2137–2139.
53. Allyn, C. L., Gossard, A. C. and Wiegmann, W. New rectifying semiconductor structure by molecular beam epitaxy. *Applied Physics Letters*, 1980. 36(5): 373–376.
54. Gehring, A. and Selberherr, S. Modeling of tunneling current and gate dielectric reliability for nonvolatile memory devices. *IEEE Transactions on Device and Materials Reliability*, 2004. 4(3): 306–319.
55. Jain, S., Neema, V., Gupta, D. and Vishvakarma, S. K. Investigation of Band-Gap Engineered Silicon-Oxide-Nitride-Oxide-Silicon Flash Memory with High-k Dielectrics in Tunnel Barrier and Its Impact on Charge Retention Dynamics. *Journal of Nanoelectronics and Optoelectronics*, 2016. 11: 6–11.
56. Jain, S., Gupta, D., Neema, V. and Vishwakarma, S. BE-SONOS flash memory along with metal gate and high- k dielectrics in tunnel barrier and its impact on charge retention dynamics. *Journal of Semiconductors*, 2016. 37(3): 1–6.
57. You, H. W., Son, J. W. and Cho, W. J. Engineering of tunnel barrier for highly integrated nonvolatile memory applications. *Applied Physics A: Materials Science and Processing*, 2011. 102(4): 921–926.
58. Padovani, A., Larcher, L., Verma, S., Pavan, P., Majhi, P., Kapur, P., Parat, K., Bersuker, G. and Saraswat, K. Statistical Modeling of Leakage Currents Through SiO₂/High- κ Dielectrics Stacks for Non-Volatile Memory Applications. *2008 IEEE International Reliability Physics Symposium*. IEEE.

2008. 616–620.
59. Verma, S. *Tunnel Barrier Engineering For Flash Memory Technology*. Ph.D. Thesis. 2010.
 60. Blomme, P., Govoreanu, B., Rosmeulen, M., Akeyar, A., Haspeslagh, L., De Vos, J., Lorenzini, M., Van Houdt, J. and De Meyer, K. High- κ Materials For Tunnel Barrier Engineering in Future Memory Technologies. *ECS Transactions*. 2006, vol. 1. 75–89.
 61. Driussi, F., Marcuzzi, S., Palestri, P. and Selmi, L. Gate current in stacked dielectrics for advanced FLASH EEPROM cells. *Proceedings of ESSDERC 2005: 35th European Solid-State Device Research Conference*. 2005, vol. 2005. 317–320.
 62. Srikantaiah, J. G. and DasGupta, A. Quantum mechanical effects in bulk MOSFETs from a compact modeling perspective: A review. *IETE Technical Review (Institution of Electronics and Telecommunication Engineers, India)*, 2012. 29(1): 3–28.
 63. Iniguez, B. and Moreno, E. G. Development of a C-continuous small-signal model for a MOS transistor in normal operation. *IEEE Transactions on Computer-Aided Design of Integrated Circuits and Systems*, 1995. 14(2): 163–166.
 64. Iniguez, B., Ferreira, L., Gentinne, B. and Flandre, D. A Physically-Based C-Continuous Fully-Depleted SOI MOSFET Model for Analog Applications. *IEEE Trans. Electron Devices*, 1996. 43(4): 568–575.
 65. Iniguez, B. and Moreno, E. G. An Improved C ∞ -Continuous Small-Geometry MOSFET Modeling for Analog Applications. *Analog Integrated Circuits and Signal Processing*, 1997. 259(13): 241–259.
 66. Miura-Mattausch, M., Feldmann, U., Rahm, A. and Bollu, M. Unified Complete Mosfet Model For Analysis Of Digital And Analog Circuits. *Computer-Aided Design, 1994., IEEE/ACM International Conference on*, 1994. 15(1): 264–267.
 67. Gildenblat, G., Member, S., Wang, H., Member, S., Chen, T.-l. and Gu, X. SP : An Advanced Surface-Potential-Based Compact MOSFET Model. *IEEE Journal of Solid-State Circuits*, 2004. 39(9): 1394–1406.
 68. Byun, Y. H., Lee, K. and Shur, M. Unified Charge Control Model and Subthreshold Current in Heterostructure Field-Effect Transistors. *IEEE Electron Device Letters*, 1990. 11(1): 50–53.

69. Maher, M. A. and Mead, C. A. A physical charge-controlled model for MOS transistors. *Advanced Research in VLSI. Proceedings of the 1987 Stanford Conference*. 1987. 211–229.
70. Cunha, A., Schneider, M. C. and Galup-Montoro, C. An Explicit Physical Model for the Long-Channel Transistor Small-Signal Parameters. *Solid State Electronics*, 1995. 38(11): 1945–1952.
71. Tsvividis, Y. *Operation and Modeling of the Mos Transistor (The Oxford Series in Electrical and Computer Engineering)*. Oxford University Press. 2004.
72. Cunha, A. I. A., Schneider, M. C. and Galup-Montoro, C. Derivation of the unified charge control model and parameter extraction procedure. *Solid-State Electronics*, 1999. 43(3): 481 – 485.
73. Iniguez, B., Jiminez, D., Roig, J., Hamid, H. A., Marsal, L. F. and Pallares, J. Explicit continuous model for long-channel undoped surrounding gate MOSFETs. *IEEE Transactions on Electron Devices*, 2005. 52(8): 1868–1873.
74. Kundert, K. *The Design's Guide to SPICE and Spectre*, Springer, chap. 2 (DC Analysis). 1995, 15–22.
75. Rios, R., Mudanai, S., Shih, W.-K. and Packan, P. An efficient surface potential solution algorithm for compact MOSFET models. *IEDM Technical Digest. IEEE International Electron Devices Meeting, 2004*. 2004. 755–758.
76. Turchetti, C. and Masetti, G. A CAD-Oriented Analytical MOSFET Model for High-Accuracy Applications. *IEEE Transactions on Computer-Aided Design of Integrated Circuits and Systems*, 1984. 3(2): 117–122.
77. Chen, T. L. and Gildenblat, G. Analytical approximation for the MOSFET surface potential. *Solid-State Electronics*, 2005. 49(2): 267–270.
78. Sacchetto, D., Ben-Jamaa, M. H., DeMicheli, G. and usuf Leblebici, Y. Fabrication and characterization of vertically stacked Gate-All-Around Si Nanowire FET arrays. *2009 Proceedings of the European Solid State Device Research Conference*. IEEE. 2009. 245–248.
79. Buddharaju, K. D., Singh, N., Rustagi, S. C., Teo, S. H. G., Wong, L. Y., Tang, L. J., Tung, C. H., Lo, G. Q., Balasubramanian, N. and Kwong, D. L. Gate-all-around Si-nanowire CMOS inverter logic fabricated using top-down approach. *European Solid-State Device Research Conference*. 2007. 303–306.

80. Oh, S.-H., Monroe, D. and Hergenrother, J. Analytic description of short-channel effects in fully-depleted double-gate and cylindrical, surrounding-gate MOSFETs. *IEEE Electron Device Letters*, 2000. 21(9): 3–6.
81. Auth, C. P. and Plummer, J. D. Scaling theory for cylindrical, fully-depleted, surrounding-gate MOSFET's. *IEEE Electron Device Letters*, 1997. 18(2): 74–76.
82. Paydavosi, N., Venugopalan, S., Chauhan, Y. S., Duarte, J. P., Jandhyala, S., Niknejad, A. M. and Hu, C. C. BSIM-SPICE Models Enable FinFET and UTB IC Designs. *IEEE Access*, 2013. 1: 201–215.
83. Jiménez, D., Iníguez, B., Suné, J., Marsal, L. F., Pallarès, J., Roig, J. and Flores, D. Continuous analytic I-V model for surrounding-gate MOSFETs. *IEEE Electron Device Letters*, 2004. 25(8): 571–573.
84. Chen, Y. and Luo, J. A comparative study of double-gate and surrounding-gate MOSFETs in strong inversion and accumulation using an analytical model. *Technical Proceedings of the 2001 International Conference on Modeling and Simulation of Microsystems*. 2001, vol. 1. 546–549.
85. Yu, B., Lu, W.-Y., Lu, H. and Taur, Y. Analytic Charge Model for Surrounding-Gate MOSFETs. *IEEE Transactions on Electron Devices*, 2007. 54(3): 492–496.
86. Jiménez, D., Sáenz, J. J., Iníguez, B., Member, S., Suñé, J., Member, S., Marsal, L. F. and Pallarès, J. Modeling of Nanoscale Gate-All-Around MOSFETs. *IEEE Electron Device Letters*, 2004. 25(5): 314–316.
87. Sadhu, J. S., Tian, H., Spila, T., Kim, J., Azeredo, B., Ferreira, P. and Sinha, S. Controllable doping and wrap-around contacts to electrolessly etched silicon nanowire arrays. *Nanotechnology*, 2014. 25(37): 375701.
88. Balestra, F., Benachir, M., Brini, J. and Ghibaudo, G. Analytical Models of Subthreshold Swing and Threshold Voltage for Thin- and Ultra-Thin-Film SOI MOSFETs. *IEEE Transactions on Electron Devices*, 1990. 37(11): 2303–2311.
89. Lee, M., Moon, T. and Kim, S. Floating Body Effect in Partially Depleted Silicon Nanowire Transistors and Potential Capacitor-Less One-Transistor DRAM Applications. *IEEE Transactions on Nanotechnology*, 2012. 11(2): 355–359.
90. Sherony, M. J., Wei, A. and Antoniadis, D. A. Effect of body-charge on fully- and partially-depleted SOI MOSFET design. *International Electron Devices Meeting. Technical Digest*. 1996. 125–128.

91. Wei, L., Chen, Z., Roy, K., Johnson, M. C., Ye, Y. and De, V. K. Design and optimization of dual-threshold circuits for low-voltage low-power applications. *IEEE Transactions on Very Large Scale Integration (VLSI) Systems*, 1999. 7(1): 16–24.
92. He, J., Liu, F., Bian, W., Feng, J., Zhang, J. and Zhang, X. An approximate carrier-based compact model for fully depleted surrounding-gate MOSFETs with a finite doping body. *Semiconductor Science and Technology*, 2007. 22(6): 671–677.
93. Duarte, J. P., Choi, S. J., Moon, D. I., Ahn, J. H., Kim, J. Y., Kim, S. and Choi, Y. K. A Universal Core Model for Multiple-Gate Field-Effect Transistors. Part I: Charge Model. *IEEE Transactions on Electron Devices*, 2013. 60(2): 840–847.
94. Duarte, J. P., Choi, S. J., Moon, D. I., Ahn, J. H., Kim, J. Y., Kim, S. and Choi, Y. K. A Universal Core Model for Multiple-Gate Field-Effect Transistors. Part II: Drain Current Model. *IEEE Transactions on Electron Devices*, 2013. 60(2): 848–855.
95. Cheralathan, M., Iannaccone, G., Sangiorgi, E. and Iiguez, B. Analytical drain current model reproducing advanced transport models in nanoscale cylindrical surrounding-gate (SRG) MOSFETs. *Journal of Applied Physics*, 2011. 110(3): 1–5.
96. Amakawa, S., Nakazato, K. and Mizuta, H. A surface-potential-based cylindrical surrounding-gate MOSFET model. (2): 3–4.
97. He, J., Bian, W., Tao, Y., Yang, S. and Tang, X. Analytic carrier-based charge and capacitance model for long-channel undoped surrounding-gate MOSFETs. *IEEE Transactions on Electron Devices*, 2007. 54(6): 1478–1485.
98. Zhou, X., Zhu, G., See, G. H., Chandrasekaran, K., Chiah, S. B. and Lim, K. Y. Unification of MOS Compact Models with the Unified Regional Modeling Approach. *J. Comput. Electron.*, 2011. 10(1-2): 121–135.
99. Dunga, M. V., Lin, C. H., Xi, X., Lu, D. D., Niknejad, A. M. and Hu, C. Modeling Advanced FET Technology in a Compact Model. *IEEE Transactions on Electron Devices*, 2006. 53(9): 1971–1978.
100. Liu, F., He, J., Zhang, J., Chen, Y. and Chan, M. A Non-Charge-Sheet Analytic Model for Symmetric Double-Gate MOSFETs With Smooth Transition Between Partially and Fully Depleted Operation Modes. *IEEE Transactions on Electron Devices*, 2008. 55(12): 3494–3502.

101. Colinge, J.-P., Lee, C.-W., Afzalian, A., Akhavan, N. D., Yan, R., Ferain, I., Razavi, P., O'Neill, B., Blake, A., White, M., Kelleher, A.-M., McCarthy, B. and Murphy, R. Nanowire transistors without junctions. *Nature Nanotechnology*, 2010. 5(3): 225–229.
102. Colinge, J. P., Kranti, A., Yan, R., Lee, C. W., Ferain, I., Yu, R., Akhavan, N. D. and Razavi, P. Junctionless Nanowire Transistor (JNT): Properties and design guidelines. *Solid-State Electronics*, 2011. 65-66(1): 33–37.
103. Winitzki, S. *Uniform Approximations for Transcendental Functions*, Berlin, Heidelberg: Springer Berlin Heidelberg. 2003, 780–789.
104. Duarte, J. P., Choi, S.-j., Moon, D.-i. and Choi, Y.-k. Simple Analytical Bulk Current Model for Long-Channel Double-Gate Junctionless Transistors. *IEEE Elect Dev Lett*, 2011. 32(6): 704–706.
105. Gildenblat, G., Li, X., Wu, W., Wang, H., Jha, A., Langevelde, R. V., Smit, G. D. J., Scholten, A. J. and Klaassen, D. B. M. PSP: An Advanced Surface-Potential-Based MOSFET Model for Circuit Simulation. *IEEE Transactions on Electron Devices*, 2006. 53(9): 1979–1993.
106. Scholten, A. J., Smit, G. D. J., Vries, B. A. D., Tiemeijer, L. F., Croon, J. A., Klaassen, D. B. M., van Langevelde, R., Li, X., Wu, W. and Gildenblat, G. The New CMC Standard Compact MOS Model PSP: Advantages for RF Applications. *IEEE Journal of Solid-State Circuits*, 2009. 44(5): 1415–1424.
107. Tsvividis, Y. and Suyama, K. MOSFET modeling for analog circuit CAD: Problems and prospects. *Custom Integrated Circuits Conference, 1993., Proceedings of the IEEE 1993*. 1993. 14.1.1–14.1.6.
108. Oana, M., Benjamin, I., David, J. and Jaume, R. Analytical Charge and Capacitance Models of Undoped Cylindrical Surrounding-Gate MOSFETs. *IEEE Transactions on Electron Devices*, 2007. 54(1): 162–165.
109. Cho, N., Yu, Y. and Hwang, S. W. A compact model of fully-depleted surrounding-gate (SG) MOSFETs with a doped body. *2008 IEEE Silicon Nanoelectronics Workshop*. 2008, 7. 1–2.
110. Ortiz-Conde, A., J. Garcia-Sanchez, F. and Malobabic, S. Analytic Solution of the Channel Potential in Undoped Symmetric Dual-Gate MOSFETs. *IEEE Trans Electron Devices*, 2005. 52(7): 1669–1672.
111. Salles, J. M., Bucher, M., Krummenacher, F. and Fazan, P. Inversion charge linearization in MOSFET modeling and rigorous derivation of the EKV compact model. *Solid-State Electronics*, 2003. 47(4): 677–683.

112. Kolodny, A., Nieh, S. T. K., Eitan, B. and Shappir, J. Analysis and Modeling of Floating-Gate EEPROM Cells. *IEEE Transactions on Electron Devices*, 1986. 33(6): 835–844.
113. Haraguchi, K., Kume, H., Ushiyama, M. and Ohkura, M. A New Simple Method for Extracting the Capacitance Coupling Coefficients of Sub-0.5-um Flash Memory Cells. *IEICE Transaction Electron*, 1999. E82-C(4): 602–606.
114. Cho, C. Y.-S. and Chen, M.-J. Improved subthreshold slope method for precise extraction of gate capacitive coupling coefficients in stacked gate and source-side injection flash memory cells. *Solid-State Electronics*, 2004. 48(7): 1189–1195.
115. Duane, R., Beug, M. F. and Mathewson, A. Novel capacitance coupling coefficient measurement methodology for floating gate nonvolatile memory devices. *IEEE Electron Device Letters*, 2005. 26(7): 507–509.
116. Rafhay, Q., Beug, M. F. and Duane, R. Extraction of the gate capacitance coupling coefficient in floating gate non-volatile memories: Statistical study of the effect of mismatching between floating gate memory and reference transistor in dummy cell extraction methods. *Solid-State Electronics*, 2007. 51(4): 585–592.
117. Liong, L. C. and Liu, P.-C. A Theoretical Model for the Current-Voltage Characteristics of a Floating-Gate EEPROM Cell. *Electron Devices, IEEE Transactions on*. 1993, vol. 40. 146–151.
118. Chung, S. S., Yih, C.-M., Wu, S. S., Chen, H. H. and Hong, G. A Spice-Compatible Flash EEPROM Model Feasible for Transient and Program/Erase Cycling Endurance Simulation. *Electron Devices Meeting, 1999. IEDM '99. Technical Digest. International*. 1999. 179–182.
119. Keeney, S., Bez, R., Cantarelli, D., Piccinini, F., Mathewson, A., Ravazzi, L. and Lombardi, C. Complete Transient Simulation of Flash EEPROM Devices. *IEEE Transactions on Electron Devices*, 1992. 39(12): 2750–2757.
120. Lanzoni, M., Suiic, J., Olivo, P. and Riccb, B. Advanced Electrical-Level Modeling of EEPROM Cells. *IEEE Transactions on Electron Devices*, 1993. 30(5): 951–957.
121. Bhattacharyya, A. Modelling of write/erase and charge retention characteristics of floating gate EEPROM devices. *Solid-State Electronics*, 1984. 27(10): 899 – 906.
122. Wong, M., Liu, D. K. Y. and Huang, S. S. W. Analysis of the Subthreshold Slope and the Linear Transconductance Techniques for the Extraction of the

- Capacitance Coupling Coefficients of Floating-Gate Devices. *IEEE Electron Device Letters*, 1992. 13(11): 566–568.
123. Duane, R., Concannon, A., O’Sullivan, P. and Mathewson, A. Advanced Numerical Modelling of Non-Volatile Memory Cells. *Solid-State Device Research Conference, 1998. Proceeding of the 28th European*. 1998. 304–307.
 124. Larcher, L., Pavan, P., Pietri, S., Albani, L. and Marmiroli, A. A New Compact DC Model of Floating Gate Memory Cells Without Capacitive Coupling Coefficients. *IEEE Transactions on Electron Devices*. 2002, vol. 49. 301–307.
 125. Larcher, L., Pavan, P., Albani, L. and Ghilardi, T. Bias and W/L dependence of capacitive coupling coefficients in floating gate memory cells. *IEEE Transactions on Electron Devices*, 2001. 48(9): 2081–2089.
 126. Larcher, L., Padovani, A., Pavan, P., Rimmaudo, I., Calderoni, A., Molteni, G., Gattel, F. and Fantini, P. *Modeling NAND Flash Memories for Circuit Simulations*, Vienna: Springer Vienna. 2007, 293–296.
 127. Larcher, L., Padovani, A., Pavan, P., Fantini, P., Calderoni, A., Mauri, A. and Benvenuti, A. Modeling nand Flash Memories for IC Design. *IEEE Electron Device Letters*, 2008. 29(10): 1152–1154.
 128. Maure, A., Canet, P., Lalande, F., Delsuc, B. and Devin, J. Flash Memory Cell Compact Modeling Using PSP Model. *2008 IEEE International Behavioral Modeling and Simulation Workshop*. 2008. 45–49.
 129. Garetto, D., Zaka, A., Quenette, V., Rideau, D., Dornel, E., Saxod, O. and Clark, W. F. Embedded nonvolatile memory study with surface potential based model. *Nanotech Conference and Expo*. 2009. 1–4.
 130. Garetto, D., Zaka, A., Manceau, J.-P., Rideau, D., Dornel, E., Clark, W. F., Schmid, A., Jaouen, H. and Leblebici, Y. Characterization and Physical Modeling of Endurance in Embedded Non-Volatile Memory Technology. *Memory Workshop (IMW), 2011 3rd IEEE International*. 2011. 1–4.
 131. Silvaco Inc., Santa Clara, CA. *ATLAS User’s Manual*, 2016.
 132. Oh, J. S., Yang, S. D., Lee, S. Y., Kim, Y. S., Kang, M. H., Lim, S. K., Lee, H. D. and Lee, G. W. 3D gate-all-around bandgap-engineered SONOS flash memory in vertical silicon pillar with metal gate. *Solid-State Electronics*, 2013. 86: 6–10.
 133. Verma, S., Pop, E., Kapur, P., Majhi, P., Parat, K. and Saraswat, K. C.

- Feasibility Study of Composite Dielectric Tunnel Barriers for Flash Memory. *65th Annual Device Research Conference*. 2007. 85–86.
134. Nitayama, A. and Aochi, H. Bit Cost Scalable (BiCS) technology for future ultra high density memories. *VLSI Technology, Systems, and Applications (VLSI-TSA), 2013 International Symposium on*. 2013. 1–2.
 135. Lime, F., Iniguez, B. and Moldovan, O. A quasi-two-dimensional compact drain-current model for undoped symmetric double-gate MOSFETs including short-channel effects. *IEEE Transactions on Electron Devices*, 2008. 55(6): 1441–1448.
 136. Roldan, J. B., Gamiz, F., Jiménez-Molinos, F., Sampedro, C., Godoy, A., García-Ruiz, F. J. and Rodriguez, N. An analytical I-V model for surrounding-gate transistors that includes quantum and velocity overshoot effects. *IEEE Transactions on Electron Devices*, 2010. 57(11): 2925–2933.
 137. Najam, F., Yu, Y. S., Cho, K. H., Yeo, K. H., Kim, D. W., Hwang, J. S., Kim, S. and Hwang, S. W. Interface trap density of gate-all-around silicon nanowire field-effect transistors with TiN gate: Extraction and compact model. *IEEE Transactions on Electron Devices*, 2013. 60(8): 2457–2463.
 138. Najam, F., Kim, S. and Yu, Y. S. Gate All Around Metal Oxide Field Transistor: Surface Potential Calculation Method including Doping and Interface Trap Charge and the Effect of Interface Trap Charge on Subthreshold Slope. *JSTS:Journal of Semiconductor Technology and Science*, 2013. 13(5): 530–537.
 139. Lin, H. C., Lin, C. I., Lin, Z. M., Shie, B. S. and Huang, T. Y. Characteristics of planar junctionless poly-Si thin-film transistors with various channel thickness. *IEEE Transactions on Electron Devices*, 2013. 60(3): 1142–1148.
 140. El Hamid, H. A., Benjamin, I. and Roig Guitart, J. R. Analytical model of the threshold voltage and subthreshold swing of undoped cylindrical gate-all-around-based MOSFETs. *IEEE Transactions on Electron Devices*, 2007. 54(3): 572–579.
 141. Yu, B., Yuan, Y., Song, J. and Taur, Y. A Two-Dimensional Analytical Solution for Short-Channel Effects in Nanowire MOSFETs. *IEEE Transactions on Electron Devices*, 2009. 56(10): 2357–2362.
 142. Abd-Elhamid, H., Benjamin, I., Jiménez, D., Roig, J., Pallares, J. and Marsal, L. F. Two-dimensional analytical threshold voltage roll-off and subthreshold swing models for undoped cylindrical gate all around MOSFET. *Solid-State Electronics*, 2006. 50(5): 805–812.

143. Zhiping, Y. and Robert W, D. Second Order Newton Iteration Method and Its Application to MOS Compact Modeling and Circuit Simulation. *VLSI Design*, 1998. 6(C): 141–146.
144. He, J., Zhang, L., Zhang, J., Ma, C., Liu, F. and Chan, M. A complete analytic surface potential-based core model for intrinsic nanowire surrounding-gate MOSFETs. *Molecular Simulation*, 2009. 35(6): 483–490.
145. Ward, D. E. and Dutton, R. W. A Charge-Oriented Model for MOS Transistor Capacitances. *IEEE Journal of Solid-State Circuits*, 1978. SC-13(5): 703–708.
146. Aurora, N. *MOSFET Modeling for VLSI Simulation*. World Scientific Publishing Co. Pte. Ltd. 2007.
147. Hamzah, A., Hamid, F. A. and Ismail, R. Explicit Continuous Charge-Based Compact Model for Heavily Doped Surrounding-Gate MOSFETs Incorporating Interface Traps and Fixed Oxide Charges. *Journal of Semiconductor and Science Technology*, 2016. 31(12): 1–13.
148. Yu, Y. S. Full-Range Analytic Drain Current Model for Nanowire Field-Effect Transistor. *Journal of Semiconductor Technology and Science*, 2013. 13(4): 361–366.
149. Yesayan, A., Jazaeri, F. and Sallese, J.-m. Charge-Based Modeling of Double-Gate and Nanowire Junctionless FETs Including Interface-Trapped Charges. *IEEE Trans Electron Devices*, 2016. 63(3): 1368–1374.
150. Najam, F., Tan, M. L. P., Ismail, R. and Seop Yu, Y. Two-dimensional (2D) transition metal dichalcogenide semiconductor field-effect transistors: the interface trap density extraction and compact model. *Semiconductor Science and Technology*, 2015. 30(7): 075010.
151. Najam, F., Lau, K. C., Lim, C. S., Yu, Y. S. and Tan, M. L. P. Metal oxide-graphene field-effect transistor: interface trap density extraction model. *Beilstein Journal of Nanotechnology*, 2016. 7: 1368–1376.
152. Bertolazzi, S., Krasnozhon, D. and Kis, A. Nonvolatile Memory Cells Based on MoS₂/Graphene Heterostructures. *ACS Nano*, 2013. 7(4): 3246–3252.
153. Hong, A. J., Song, E. B., Yu, H. S., Allen, M. J., Kim, J., Fowler, J. D., Wassei, J. K., Park, Y., Wang, Y., Zou, J., Kaner, R. B., Weiller, B. H. and Wang, K. L. Graphene Flash Memory. *ACS Nano*, 2011. 5(10): 7812–7817.

APPENDIX A

PARAMETER OPTIMIZATION OF ASYMMETRIC VARIOT

Table A.1: Parameters and data for SiO₂/Si₃N₄ extracted from TCAD simulation.

EOT (nm)	T _{ox} (nm)	T _{hk} (nm)	V _{prog} (V)	V _{read_dis} (V)	V _{ret} (V)	V _{tr} (V)	V _{fn} (V)
4	1	5.8	3.7	2.1	-2.3	8.0	12.8
	2	3.8	3.6	1.9	-1.5	4.0	6.4
	3	1.9	4.8	1.8	-0.8	2.7	4.3
	4	0.0	4.7	1.7	0	2.0	3.2
5	1	7.7	4.5	2.5	-3.2	10.0	16.0
	2	5.8	4.5	2.4	-3.9	5.0	8.0
	3	3.8	6.0	2.3	-3.9	3.3	5.3
	4	1.9	6	2.5	-3.2	2.5	4.0
	5	0.0	5.9	3.2	-1.7	2.0	3.2
6	1	9.6	5.4	3.0	-3.4	12.0	19.2
	2	7.7	5.3	2.9	-4.0	6.0	9.6
	3	5.8	7.2	2.8	-4.5	4.0	6.4
	4	3.8	7.1	3.0	-4.6	3.0	4.8
	5	1.9	7.0	3.8	-4.5	2.4	3.8
	6	0.0	7.0	3.8	-4.2	2.0	3.2
7	1	11.5	6.3	3.5	-3.8	14.0	22.4
	2	9.6	6.2	3.3	-4.0	7.0	11.2
	3	7.7	8.4	3.3	-4.2	4.7	7.5
	4	5.7	8.3	3.5	-5.1	3.5	5.6
	5	3.8	8.1	4.4	-5.2	2.8	4.5
	6	1.9	8.2	4.4	-4.9	2.3	3.7
	7	0.0	8.2	4.4	-4.6	2.0	3.2
8	1	13.5	7.2	4.0	-4.3	16.0	25.6
	2	11.5	7.1	3.8	-4.2	8.0	12.8
	3	9.6	9.6	3.7	-4.3	5.3	8.5
	4	7.7	9.5	4.0	-4.6	4.0	6.4
	5	5.8	9.3	5.0	-5.7	3.2	5.1
	6	3.8	9.4	5.0	-5.8	2.7	4.3
	7	1.9	9.4	5.0	-5.5	2.3	3.7
	8	0.0	9.4	5.0	-5.1	2.0	3.2

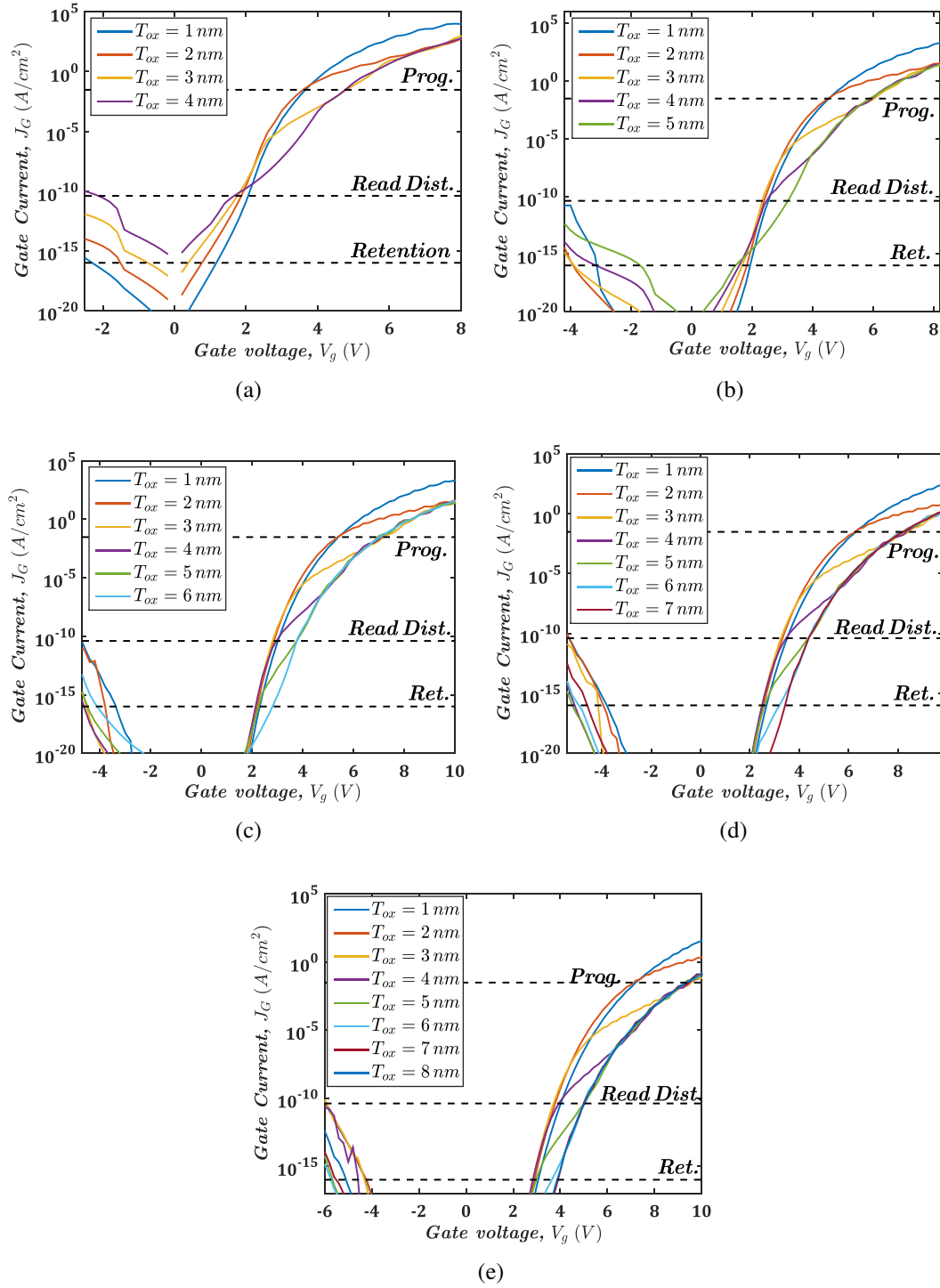


Figure A.1: $J_g - V_g$ characteristics of SiO₂/Si₃N₄ for EOT (a) 4nm (b) 5nm (c) 6nm (d) 7nm and (e) 8nm.

Table A.2: Parameters and data for SiO₂/Al₂O₃ extracted from TCAD simulation.

EOT (nm)	T _{ox} (nm)	T _{hk} (nm)	V _{prog} (V)	V _{read_dis} (V)	V _{ret} (V)	V _{tr} (V)	V _{fn} (V)
4	1	7.2	5.5	3.1	-4.6	9.6	12.8
	2	4.8	4.7	2.9	-4.1	4.8	6.4
	3	2.4	4.8	2.5	-1.8	3.2	4.3
	4	0.0	4.8	1.7	0	2.4	3.2
5	1	9.5	6.7	4.1	-5.3	12.0	16.0
	2	7.2	5.8	3.3	-5.3	6.0	8.0
	3	4.8	6.0	3.1	-5.0	4.0	5.3
	4	2.4	6.0	2.8	-4.3	3.0	4.0
	5	0.0	5.9	3.2	-1.8	2.4	3.2
6	1	11.9	8.2	4.9	-6.1	14.4	19.2
	2	9.5	6.9	4.3	-6.0	7.2	9.6
	3	7.2	7.2	4.0	-6.2	4.8	6.4
	4	4.8	7.2	3.7	-5.6	3.6	4.8
	5	2.4	7.2	3.8	-4.9	2.9	3.8
	6	0.0	7.1	3.8	-4.2	2.4	3.2
7	1	14.3	9.4	5.7	-6.9	16.8	22.4
	2	11.9	8.1	5.0	-6.9	8.4	11.2
	3	9.5	8.3	4.6	-6.9	5.6	7.5
	4	7.2	8.4	4.3	-7.0	4.2	5.6
	5	4.8	8.2	4.4	-6.5	3.4	4.5
	6	2.4	8.3	4.4	-5.5	2.8	3.7
	7	0.0	8.2	4.4	-4.6	2.4	3.2
8	1	16.7	10.8	6.5	-7.7	19.2	25.6
	2	14.3	9.2	5.7	-7.7	9.6	12.8
	3	11.9	9.5	5.2	-7.7	6.4	8.5
	4	9.5	9.5	4.9	-7.7	4.8	6.4
	5	7.2	9.4	5.0	-7.8	3.8	5.1
	6	4.8	9.4	5.0	-7.2	3.2	4.3
	7	2.4	9.4	5.0	-6.2	2.7	3.7
	8	0.0	9.5	5.0	-5.1	2.4	3.2

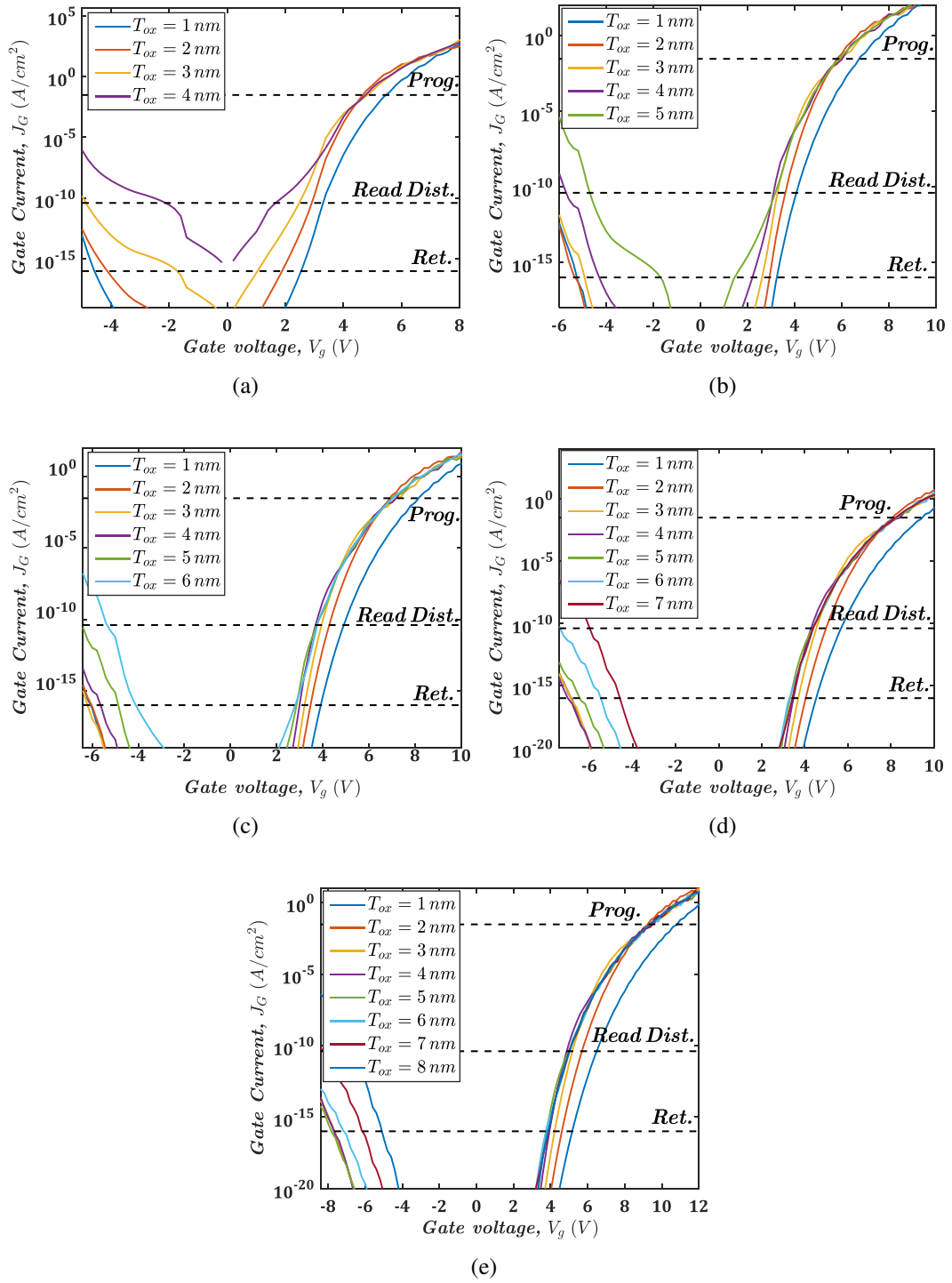


Figure A.2: $J_g - V_g$ characteristics of SiO₂/Al₂O₃ for EOT (a) 4nm (b) 5nm (c) 6nm (d) 7nm and (e) 8nm.

Table A.3: Parameters and data for SiO₂/HfO₂ extracted from TCAD simulation.

EOT (nm)	T _{ox} (nm)	T _{hk} (nm)	V _{prog} (V)	V _{read_dis} (V)	V _{ret} (V)	V _{tr} (V)	V _{fn} (V)
4	1	14.6	3.0	1.7	-2.2	6.0	12.8
	2	9.7	2.8	1.5	-3.5	3.0	6.4
	3	4.9	4.9	1.5	-3.1	2.0	4.3
	4	0.0	4.8	1.7	0.0	1.5	3.2
5	1	19.5	3.8	2.1	-2.7	7.5	16.0
	2	14.6	3.5	1.8	-3.5	3.8	8.0
	3	9.7	6.4	1.8	-4.1	2.5	5.3
	4	4.9	6.3	2.2	-4.5	1.9	4.0
	5	0.0	5.9	3.2	-1.7	1.5	3.2
6	1	24.4	4.5	2.5	-3.2	9.0	19.2
	2	19.5	4.2	2.2	-3.5	4.5	9.6
	3	14.6	7.5	2.2	-3.7	3.0	6.4
	4	9.7	7.3	2.7	-4.8	2.3	4.8
	5	4.9	7.0	3.9	-4.9	1.8	3.8
	6	0.0	7.0	3.8	-4.1	1.5	3.2
7	1	29.2	5.2	2.9	-3.5	10.5	22.4
	2	24.4	5.0	2.6	-3.6	5.3	11.2
	3	19.5	8.7	2.5	-4.0	3.5	7.5
	4	14.6	8.4	3.1	-4.4	2.6	5.6
	5	9.7	8.0	4.5	-5.4	2.1	4.5
	6	4.9	8.2	4.4	-5.6	1.8	3.7
	7	0.0	8.2	4.4	-4.6	1.5	3.2
8	1	34.1	5.9	3.3	-3.9	12.0	25.6
	2	29.2	5.6	2.9	-3.9	6.0	12.8
	3	24.4	9.9	2.9	-3.9	4.0	8.5
	4	19.5	9.6	3.5	-4.5	3.0	6.4
	5	14.6	9.2	5.0	-5.1	2.4	5.1
	6	9.7	9.2	5.0	-6.0	2.0	4.3
	7	4.9	9.5	5.0	-6.6	1.7	3.7
	8	0.0	9.4	5.0	-5.2	1.5	3.2

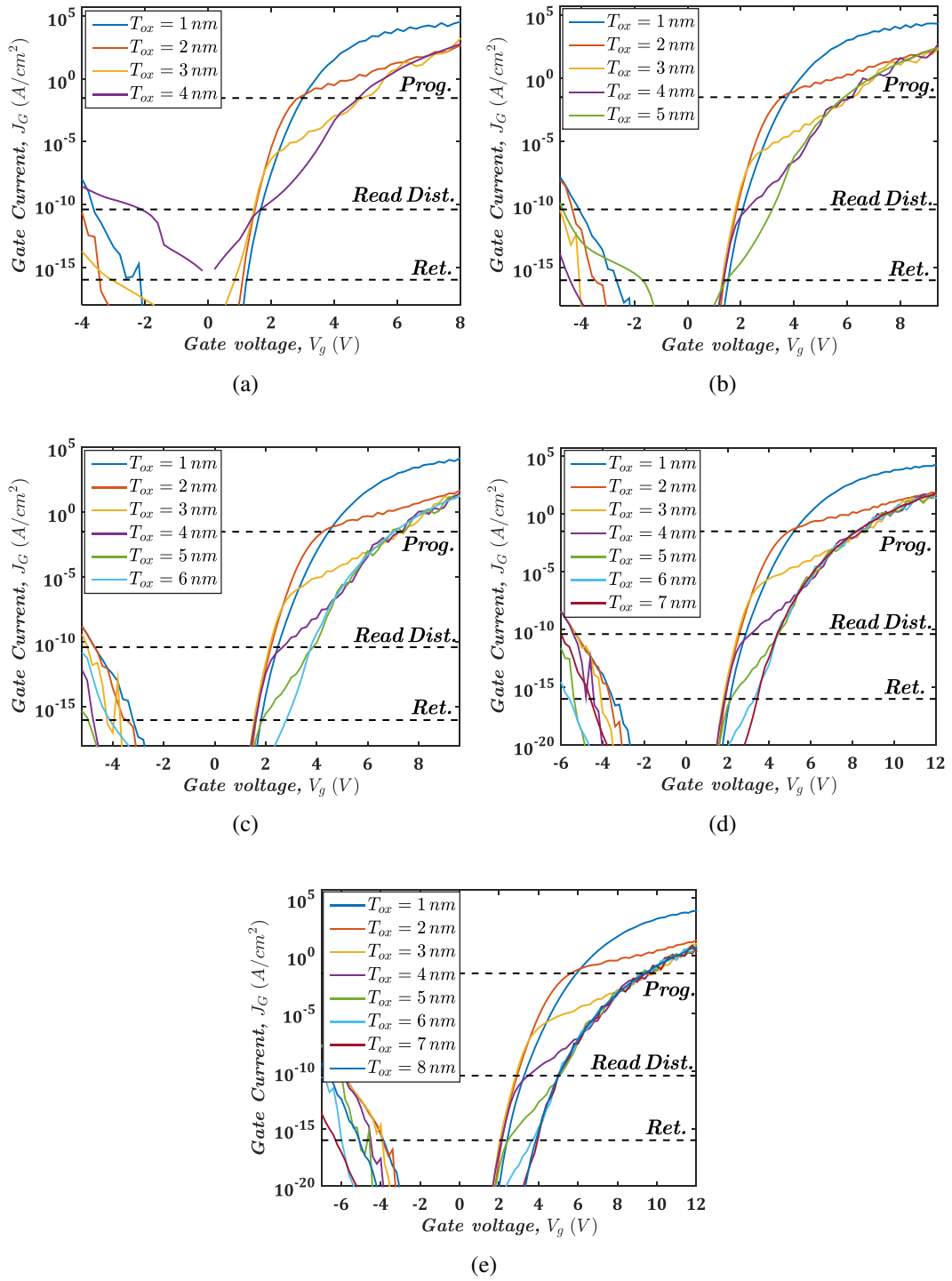


Figure A.3: $J_g - V_g$ characteristics of SiO₂/HfO₂ for EOT (a) 4nm (b) 5nm (c) 6nm (d) 7nm and (e) 8nm.

Table A.4: Parameters and data for SiO₂/ZrO₂ extracted from TCAD simulation.

EOT (nm)	T _{ox} (nm)	T _{hk} (nm)	V _{prog} (V)	V _{read_dis} (V)	V _{ret} (V)	V _{tr} (V)	V _{fn} (V)
4	1	19.2	3.0	1.7	-2.6	5.6	12.8
	2	12.8	2.8	1.4	-3.5	2.8	6.4
	3	6.4	4.9	1.4	-4.0	1.9	4.3
	4	0.0	4.8	1.7	0.0	1.4	3.2
5	1	25.4	3.7	2.1	-3.2	7.0	16.0
	2	19.2	3.4	1.8	-3.8	3.5	8.0
	3	12.8	6.2	1.7	-4.4	2.3	5.3
	4	6.4	6.1	2.2	-4.8	1.8	4.0
	5	0.0	5.9	3.2	-1.7	1.4	3.2
6	1	32.1	4.5	2.5	-3.6	8.4	19.2
	2	25.6	4.1	2.1	-3.9	4.2	9.6
	3	19.2	7.2	2.1	-4.4	2.8	6.4
	4	12.8	7.3	2.6	-5.0	2.1	4.8
	5	6.4	7.1	3.8	-5.5	1.7	3.8
	6	0.0	7.2	3.8	-4.1	1.4	3.2
7	1	38.5	5.2	2.9	-4.0	9.8	22.4
	2	32.1	4.8	2.5	-4.0	4.9	11.2
	3	25.6	8.5	2.4	-4.3	3.3	7.5
	4	19.2	8.4	3.1	-4.9	2.5	5.6
	5	12.8	8.2	4.5	-5.3	2.0	4.5
	6	6.4	8.3	4.4	-6.2	1.6	3.7
	7	0.0	8.2	4.4	-4.6	1.4	3.2
8	1	44.9	5.7	3.3	-4.4	11.2	25.6
	2	38.5	5.4	2.8	-4.4	5.6	12.8
	3	32.1	9.8	2.7	-4.4	3.7	8.5
	4	25.6	9.6	3.5	-4.9	2.8	6.4
	5	19.2	9.4	5.1	-5.4	2.2	5.1
	6	12.8	9.4	5.0	-6.2	1.9	4.3
	7	6.4	9.4	5.0	-7.0	1.6	3.7
	8	0.0	9.4	5.0	-5.1	1.4	3.2

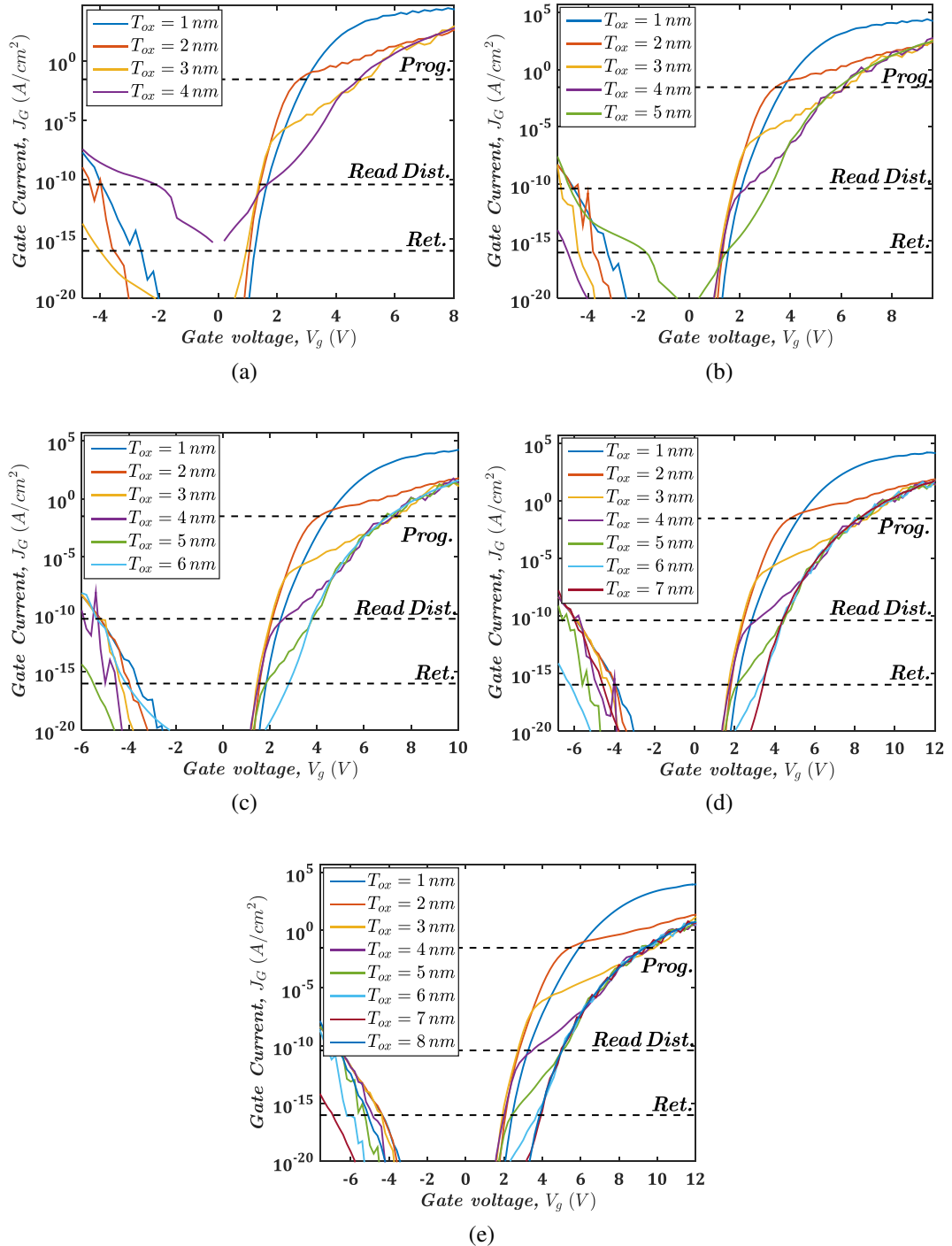


Figure A.4: $J_g - V_g$ characteristics of SiO₂/ZrO₂ for EOT (a) 4nm (b) 5nm (c) 6nm (d) 7nm and (e) 8nm.

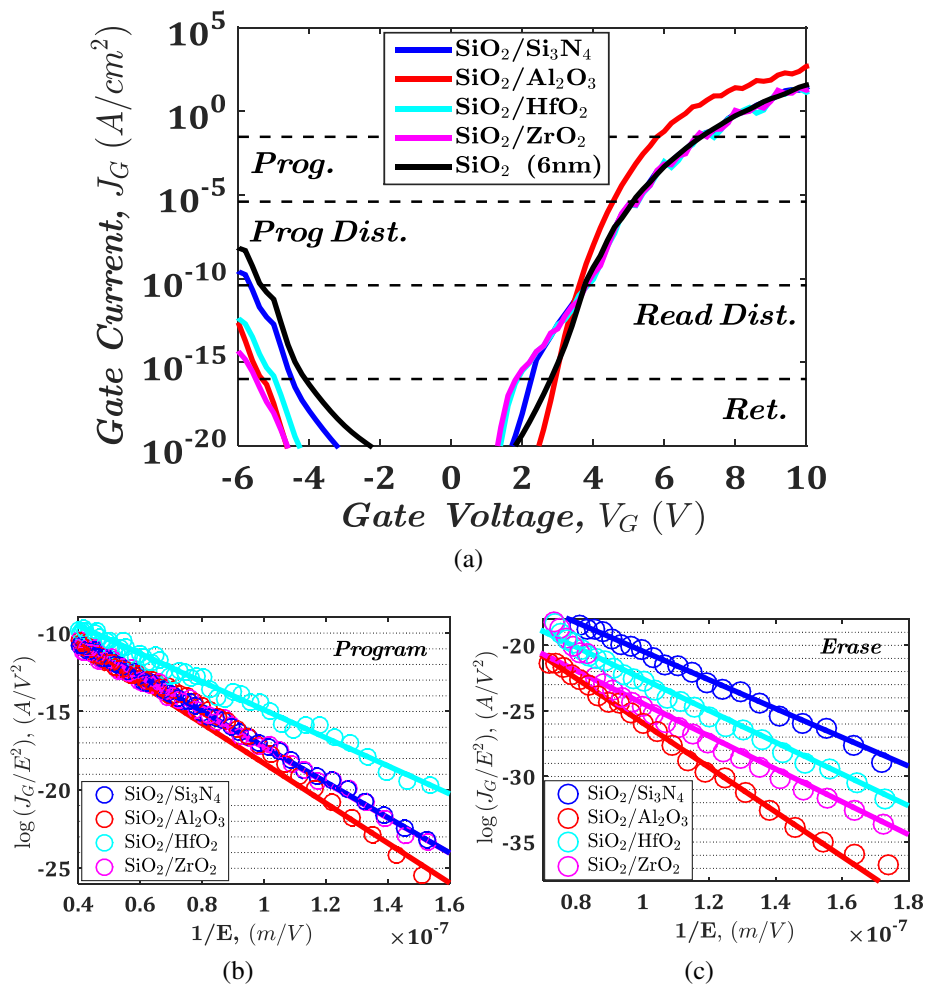


Figure A.5: (a) JV characteristics for the optimized parameters of all asymmetric VARIOTs conducted. F-N plot of all asymmetric VARIOTs conducted for (b) programming and (c) erase operations.

APPENDIX B

DERIVATION OF CHARGE-BASED COMPACT MODEL

B.1 Charge-Based Compact Model for Partially-Depleted GAANWFETs

Derivation for UCCM Expression;

Poisson's equation in 1-D for a semiconductor system given as

$$\nabla^2 \phi = -\frac{\rho}{\epsilon_{si}} = -\frac{q(p - n + N_D^+ - N_A^-)}{\epsilon_{si}} \quad (\text{B.1})$$

$$\frac{1}{r} \frac{d}{dr} \left(r \frac{d\phi(r)}{dr} \right) = \frac{qN_A}{\epsilon_{si}} \left(1 + \exp \left(\frac{\phi(r) - 2\phi_f - V}{\phi_t} \right) \right) \quad (\text{B.2})$$

$$r \frac{d\phi(r)}{dr} = \frac{qN_A r^2}{2\epsilon_{si}} + \int_0^r \left(\frac{qN_A}{\epsilon_{si}} \exp \left(\frac{\phi_0 - 2\phi_f - V}{\phi_t} \right) \right) r \cdot dr \quad (\text{B.3})$$

given the boundary condition in GAANWFET as

$$\left. \frac{d\phi}{dr} \right|_{r=0} = 0, \quad \phi(r=0) = \phi_0, \quad \phi(r=R) = \phi_s \quad (\text{B.4})$$

The Poisson has no analytical solution due to potential being dependence to r . In order to integrate the expression, Following [26], it need to be initially solved for weak

inversion and fully-depleted case before latter the moderate and the strong inversion are included. In weak inversion the potential at the surface and the center body is same ($\phi_0 = \phi_s$), similar goes to its carrier concentration ($n_0 = n_s$).

$$\frac{1}{r} \frac{d}{dr} \left(r \frac{d\phi(r)}{dr} \right) = \frac{qN_A}{\epsilon_{si}} \left(1 + \exp \left(\frac{\phi_0 - 2\phi_f - V}{\phi_t} \right) \right) \quad (\text{B.5})$$

Perform the 1st integral for any value of r

$$r \frac{d\phi(r)}{dr} = \int_0^r \frac{qN_A}{\epsilon_{si}} \left(1 + \exp \left(\frac{\phi_0 - 2\phi_f - V}{\phi_t} \right) \right) r \cdot dr \quad (\text{B.6})$$

$$\frac{d\phi(r)}{dr} = \frac{qN_A r}{2\epsilon_{si}} + \frac{qn_0 r}{2\epsilon_{si}} \quad (\text{B.7})$$

Multiply with R/R

$$\frac{d\phi(r)}{dr} = \left(\frac{qN_A R}{2R\epsilon_{si}} + \frac{qn_0 R}{2R\epsilon_{si}} \right) \cdot r \quad (\text{B.8})$$

By replacing $Q_{dep} = qN_A R/2$ and $Q_m = qn_0 R/2$

$$d\phi(r) = \left(\frac{Q_{dep} + Q_m}{R\epsilon_{si}} \right) r \cdot dr \quad (\text{B.9})$$

Replace $r \cdot dr$ into Poisson equation without the weak inversion assumption

$$r \frac{d\phi(r)}{dr} = \frac{qN_A r^2}{2\epsilon_{si}} + \int_{\phi_0}^{\phi} \left(\frac{qN_A}{\epsilon_{si}} \exp \left(\frac{\phi(r) - 2\phi_f - V}{\phi_t} \right) \right) \left(\frac{R\epsilon_{si}}{Q_{dep} + Q_m} \right) \cdot d\phi(r) \quad (\text{B.10})$$

Solve for RHS from $\phi(r=0) = \phi_0$ to $\phi(r=r) = \phi$ and using the boundary condition of $\left. \frac{d\phi}{dr} \right|_{r=R} = -E_s$, the Poisson can be obtained as

$$\begin{aligned} \left. \frac{d\phi}{dr} \right|_{r=R} &= \frac{Q_{dep}}{\epsilon_{si}} + \frac{\phi_t}{R} \left(\frac{2Q_{dep}}{Q_{dep} + Q_m} \right) \left(1 - \exp \left(\frac{\phi_0 - \phi_s}{\phi_t} \right) \right) \\ &\times \exp \left(\frac{\phi_s - 2\phi_f - V}{\phi_t} \right) \end{aligned} \quad (\text{B.11})$$

The second term is actually the total mobile charge, Q_m at the channel interface

$$\frac{Q_m}{\epsilon_{si}} = \frac{\phi_t}{R} \left(\frac{2Q_{dep}}{Q_{dep} + Q_m} \right) \left(1 - \exp \left(\frac{\phi_0 - \phi_s}{\phi_t} \right) \right) \cdot \exp \left(\frac{\phi_s - 2\phi_f - V}{\phi_t} \right) \quad (\text{B.12})$$

Using full-depletion approximation of $(\phi_0 - \phi_s)/\phi_t = qN_A R^2/4\epsilon_{si}$. Taking logarithm to both side and solve for ϕ_s

$$\begin{aligned} \phi_s &= 2\phi_f + V + \phi_t \ln \left(\frac{R}{2\phi_t \epsilon_{si}} \right) - \phi_t \ln \left(1 - \exp \left(-\frac{RQ_{dep}}{2\phi_t \epsilon_{si}} \right) \right) \\ &+ \phi_t \ln(Q_m) + \phi_t \ln \left(1 + \frac{Q_m}{Q_{dep}} \right) \end{aligned} \quad (\text{B.13})$$

However, Q_{dep} in the last term will results in overestimation of the surface potential in strong inversion region due to the weak inversion approximation. Therefore, following [26], parameter Q_{dep} is changed to $C_{ox}\phi_t/H$.

$$\begin{aligned} \phi_s &= 2\phi_f + V + \phi_t \ln \left(\frac{R}{2\phi_t \epsilon_{si}} \right) - \phi_t \ln \left(1 - \exp \left(-\frac{RQ_{dep}}{2\phi_t \epsilon_{si}} \right) \right) \\ &+ \phi_t \ln(Q_m) + \phi_t \ln \left(1 + H \frac{Q_m}{C_{ox}\phi_t} \right) \end{aligned} \quad (\text{B.14})$$

Replacing the surface potential expression into Gauss's law that enclosed across the gate stack

$$C_{ox} (V_g - \Delta\varphi - \phi_s) = Q_{dep} + Q_m - Q_f + qD_{it}\phi_s \quad (\text{B.15})$$

$$V_g - V_{th} - \Delta V_{th} - \eta V = \frac{Q_m}{C_{ox}} + \eta\phi_t \ln\left(\frac{Q_m}{Q_0}\right) + \eta\phi_t \ln\left(1 + \frac{Q_m}{Q_0}\right) \quad (\text{B.16})$$

where $Q_0 = C_{ox}\phi_t/H$ with

$$V_{th} = \Delta\varphi + 2\eta\phi_f + \frac{Q_{dep}}{C_{ox}} - \frac{Q_f}{C_{ox}} - \eta\phi_t \ln\left(\frac{4\phi_t\epsilon_{si}Q_{dep}}{RQ_0}\right) \quad (\text{B.17})$$

and

$$\Delta V_{th} = -\eta\phi_t \ln\left(\frac{1}{Q_0}\right) \quad (\text{B.18})$$

Derivation for partial-depletion conduction;

$$\frac{1}{r} \frac{d}{dr} \left(r \frac{d\phi_2(r)}{dr} \right) = \frac{qN_A}{\epsilon_{si}} \quad (\text{B.19})$$

In partial-depletion conduction, the boundary conditions are given as

$$\frac{d\phi_2(r = r_{dep})}{dr} = 0, \quad \phi_2(r = r_{dep}) = 0, \quad \phi_2(r = R) = \phi_2. \quad (\text{B.20})$$

Solving for its first derivative

$$\frac{1}{r} \frac{d}{dr} \left(r \frac{d\phi_2(r)}{dr} \right) \left(\frac{d\phi_2(r)}{dr} \right) = \frac{qN_A}{\varepsilon_{si}} \left(\frac{d\phi_2(r)}{dr} \right) \quad (\text{B.21})$$

$$\frac{1}{r} \frac{d}{dr} \left(r \frac{d\phi_2(r)}{dr} \right) \left(\frac{d\phi_2(r)}{dr} \right) = \frac{qN_A}{\varepsilon_{si}} \left(\frac{d\phi_2(r)}{dr} \right) \quad (\text{B.22})$$

$$\left(\frac{d\phi_2(r)}{dr} \right)^2 = \int_{r_{dep}}^R \frac{qN_A}{\varepsilon_{si}} \cdot d\phi_2(r) \quad (\text{B.23})$$

$$\left. \frac{d\phi_2}{dr} \right|_{r=R} = \sqrt{\frac{qN_A}{\varepsilon_{si}} \cdot \phi_2} = \sqrt{\frac{qN_A}{\varepsilon_{si}} \cdot \phi_c}; \quad (\text{B.24})$$

Solution for channel charge;

$$Q_{ch} = -2\pi R \int_0^L Q_m dy = -\mu \frac{(2\pi R)^2}{I_{ds}} \int_0^{V_d} Q_m^2 dV \quad (\text{B.25})$$

$$Q_{ch} = \mu \frac{(2\pi R)^2}{I_{ds}} \left[\frac{Q_m}{3C_{ox}} + \frac{\eta\phi_t Q_m^2}{2} + \eta\phi_t \left(Q_0^2 \ln(Q_m + Q_0) + \frac{Q_m^2}{2} - Q_0 Q_m \right) \right] \Bigg|_{Q_{m0}}^{Q_{mL}} \quad (\text{B.26})$$

Solution for drain charge;

$$Q_d = -2\pi R \int_0^L \frac{y}{L} Q_m \frac{dy}{dQ_m} dQ_m \quad (\text{B.27})$$

from current continuity equation

$$I_{ds} = 2\pi R\mu Q_m \frac{dV}{dy} = 2\pi R\mu Q_m \frac{dV}{dQ_m} \cdot \frac{dQ_m}{dy} \quad (\text{B.28})$$

replacing dy/dQ_m of the current continuity equation into Q_d with dV/dQ_m is differentiate from UCCM expression

$$Q_d = -\frac{(2\pi R)^2}{I_{ds}} \int_0^L \frac{y}{L} Q_m^2 \left[-\frac{1}{C_{ox}} - \eta\phi_t \left(\frac{1}{Q_m} + \frac{1}{Q_m + Q_0} \right) \right] dQ_m \quad (\text{B.29})$$

the distance along channel y is again obtained from current continuity equation by rearranging it to be in a function of dy as

$$dy = \frac{2\pi R\mu}{I_{ds}} Q_m \left[-\frac{1}{C_{ox}} - \eta\phi_t \left(\frac{1}{Q_m} + \frac{1}{Q_m + Q_0} \right) \right] \cdot dQ_m \quad (\text{B.30})$$

integrating y from 0 to distance of y and Q_m from Q_{m0} to Q_m , distance y is obtained

$$y = \frac{2\pi R\mu}{I_{ds}} \left[\frac{Q_m^2 - Q_{m0}^2}{2C_{ox}} + \eta\phi_t \left(2(Q_m - Q_{m0}) - Q_0 \cdot \log \left[\frac{Q_m + Q_0}{Q_{m0} + Q_0} \right] \right) \right] \quad (\text{B.31})$$

replace y into expression Q_d

$$Q_d = \int_{Q_{m0}}^{Q_{mL}} -\frac{((2\pi R)^3 \mu^2)}{I_{ds}^2 L} \cdot \left[Q_m^2 \left(\eta\phi_t \left(2(Q_m - Q_{m0}) - Q_0 \log \left(\frac{Q_m + Q_0}{Q_0 + Q_{m0}} \right) \right) + \frac{Q_m^2 - Q_{m0}^2}{2C_{ox}} \right) \left(\eta\phi_t \left(\frac{1}{Q_m + Q_0} + \frac{1}{Q_m} \right) + \frac{1}{C_{ox}} \right) \right] dQ \quad (\text{B.32})$$

Solution to integration

$$\begin{aligned}
Q_d = & \frac{-4\pi^3 R^3 \mu^2}{C_{ox}^2 I_{ds}^2 L} \left[\frac{Q_{m0}}{90} (12Q_{m0}^4 + 30\eta C_{ox} Q_0^3 \phi_t + 75\eta C_{ox} Q_{m0}^3 \phi_t) \right] \\
& + 40\eta C_{ox} Q_{m0}^2 \phi_t (-2Q_0 + 3\eta C_{ox} \phi_t) - 15\eta C_{ox} Q_0 Q_{m0} \phi_t \\
& (Q_0 + 18\eta C_{ox} \phi_t) + \frac{1}{90} Q_{mL} (18Q_{mL}^4 + 135\eta C_{ox} Q_{mL}^3 \phi_t - 10Q_{mL}^2 \\
& (3Q_{m0}^2 + 12\eta C_{ox} Q_{m0} \phi_t + \eta C_{ox} \phi_t (Q_0 - 24\eta C_{ox} \phi_t)) + \\
& 30\eta C_{ox} Q_0 \phi_t (-Q_0^2 + 3Q_{m0} (Q_{m0} + 4\eta C_{ox} \phi_t)) - 15\eta C_{ox} Q_{mL} \phi_t \\
& (-Q_0^2 + 6\eta C_{ox} Q_0 \phi_t + 6Q_{m0} (Q_{m0} + 4\eta C_{ox} \phi_t))) \\
& - \frac{1}{3} \eta C_{ox} Q_0^2 \phi_t (-Q_0^2 + 3Q_{m0} (Q_{m0} + 4\eta C_{ox} \phi_t)) \log(Q_0 + Q_{mL}) \\
& + \frac{2}{3} \eta C_{ox} Q_0 Q_{mL} \phi_t (-Q_{mL}^2 + 3\eta C_{ox} Q_0 \phi_t - 3\eta C_{ox} Q_{mL} \phi_t) \cdot \\
& \log\left(\frac{Q_0 + Q_{mL}}{Q_0 + Q_{m0}}\right) - \eta^2 C_{ox}^2 Q_0^3 \phi_t^2 \log\left(\frac{Q_0 + Q_{mL}}{Q_0 + Q_{m0}}\right)^2 \\
& + \frac{1}{3} \eta C_{ox} Q_0^2 \phi_t \cdot (-Q_0^2 + 3Q_{m0} (Q_{m0} + 4\eta C_{ox} \phi_t)) \\
& \log(Q_0 + Q_{m0})
\end{aligned} \tag{B.33}$$

B.2 Charge-Based Compact Model for Junctionless Nanowire Transistor

Derivation for UCCM Expression;

Poisson's equation in 1-D for a semiconductor system given as

$$\nabla^2 \phi = -\frac{\rho}{\epsilon_{si}} = -\frac{q(p - n + N_D^+ - N_A^-)}{\epsilon_{si}} \tag{B.34}$$

$$\frac{1}{r} \frac{d}{dr} \left(r \frac{d\phi(r)}{dr} \right) = -\frac{qN_D}{\epsilon_{si}} \left(1 - \exp\left(\frac{\phi(r) - V}{\phi_t}\right) \right) \tag{B.35}$$

$$r \frac{d\phi(r)}{dr} = -\frac{qN_D r^2}{2\epsilon_{si}} + \int_0^r \left(\frac{qN_D}{\epsilon_{si}} \exp\left(\frac{\phi_0 - V}{\phi_t}\right) \right) r \cdot dr \tag{B.36}$$

given the boundary condition in JNT as

$$\left. \frac{d\phi}{dr} \right|_{r=0} = 0, \quad \phi(r=0) = \phi_0, \quad \phi(r=R) = \phi_s \quad (\text{B.37})$$

The Poisson has no analytical solution due to potential being dependence to r . In order to integrate the expression, Following [26], it need to be initially solved for weak inversion and fully-depleted case. In weak inversion the potential at the surface and the center body is same ($\phi_0 = \phi_s$), similar goes to its carrier concentration ($n_0 = n_s$).

$$\frac{1}{r} \frac{d}{dr} \left(r \frac{d\phi(r)}{dr} \right) = -\frac{qN_D}{\epsilon_{si}} \left(1 - \exp \left(\frac{\phi_0 - V}{\phi_t} \right) \right) \quad (\text{B.38})$$

Perform the 1st integral for any value of r

$$r \frac{d\phi(r)}{dr} = \int_0^r \frac{qN_D}{\epsilon_{si}} \left(-1 + \exp \left(\frac{\phi_0 - V}{\phi_t} \right) \right) r \cdot dr \quad (\text{B.39})$$

$$\frac{d\phi(r)}{dr} = -\frac{qN_A r}{2\epsilon_{si}} + \frac{qn_0 r}{2\epsilon_{si}} \quad (\text{B.40})$$

Multiply with R/R

$$\frac{d\phi(r)}{dr} = \left(-\frac{qN_A R}{2R\epsilon_{si}} + \frac{qn_0 R}{2R\epsilon_{si}} \right) \cdot r \quad (\text{B.41})$$

By replacing $Q_{dep} = qN_D R/2$ and $Q_m = qn_0 R/2$

$$d\phi(r) = \left(\frac{-Q_{dep} + Q_m}{R\epsilon_{si}} \right) r \cdot dr \quad (\text{B.42})$$

Replace $r \cdot dr$ into Poisson equation without the weak inversion assumption

$$r \frac{d\phi(r)}{dr} = -\frac{qN_D r^2}{2\epsilon_{si}} + \int_{\phi_0}^{\phi} \left(\frac{qN_D}{\epsilon_{si}} \exp\left(\frac{\phi(r) - V}{\phi_t}\right) \right) \left(\frac{R\epsilon_{si}}{-Q_{dep} + Q_m} \right) \cdot d\phi(r) \quad (\text{B.43})$$

Solve for RHS from $\phi(r=0) = \phi_0$ to $\phi(r=r) = \phi$ and using the boundary condition of $\left. \frac{d\phi}{dr} \right|_{r=R} = -E_s$, the Poisson can be obtained as

$$\begin{aligned} \left. \frac{d\phi}{dr} \right|_{r=R} &= -\frac{Q_{dep}}{\epsilon_{si}} + \frac{\phi_t}{R} \left(\frac{2Q_{dep}}{-Q_{dep} + Q_m} \right) \left(1 - \exp\left(\frac{\phi_0 - \phi_s}{\phi_t}\right) \right) \\ &\quad \times \exp\left(\frac{\phi_s - V}{\phi_t}\right) \end{aligned} \quad (\text{B.44})$$

The second term is actually the total mobile charge, Q_m at the channel interface

$$\frac{Q_m}{\epsilon_{si}} = \frac{\phi_t}{R} \left(\frac{2Q_{dep}}{-Q_{dep} + Q_m} \right) \left(1 - \exp\left(\frac{\phi_0 - \phi_s}{\phi_t}\right) \right) \cdot \exp\left(\frac{\phi_s - V}{\phi_t}\right) \quad (\text{B.45})$$

The potential relation is replaced by using parabolic potential profile of $\phi(r) = (\phi_s - \phi_0) r^2/R^2 + \phi_0$, where $(\phi_s - \phi_0)/\phi_t = (-Q_{dep} + Q_m)/Q_{sc}$. Taking logarithm to both side and solve for ϕ_s

$$\begin{aligned} \phi_s &= \phi_t \ln \left(\frac{-Q_{dep} + Q_m}{Q_{dep} Q_{sc}} \right) + \phi_t \ln(Q_m) + V \\ &\quad - \phi_t \ln \left(1 - \exp \left[- \left(\frac{-Q_{dep} + Q_m}{Q_{sc}} \right) \right] \right). \end{aligned} \quad (\text{B.46})$$

Given Gauss's law at channel interface as

$$C_{ox} (V_g - V_{FB} - \eta\phi_s) = -Q_{dep} + Q_m \quad (\text{B.47})$$

where η is the interface trap parameter and by substituting the surface potential into the Gauss's law, the UCCM expression for JNT is finally deduced as

$$V_g - V_{th} - \eta V = \frac{Q_m}{C_{ox}} + \eta\phi_t \ln\left(\frac{Q_m}{Q_{sc}}\right) - \eta\phi_t \ln\left(\frac{Q_{dep} [1 - \exp(-Q_T/Q_{sc})]}{Q_T}\right) \quad (\text{B.48})$$

The total charge, Q_T is inferred as $-Q_{dep} + Q_m$ and threshold voltage, $V_{th} = V_{FB} - Q_{dep}/C_{ox}$.

Solution to drain charge Q_d

$$Q_d = Q_{dDP} + Q_{dC} \quad (\text{B.49})$$

$$Q_d = -2\pi R \int_0^L \frac{y}{L} Q_{DP} \frac{dy}{dQ_{DP}} dQ_{DP} - 2\pi R \int_0^L \frac{y}{L} Q_C \frac{dy}{dQ_C} dQ_C \quad (\text{B.50})$$

Solution to integration of Equation (5.73)

$$\begin{aligned} Q_{dDP} = & - \frac{(Q_{DPL} - Q_{DP0})^2 (12Q_{DPL}^3 + 24Q_{DPL}^2 Q_{DP0} + 16Q_{DPL} Q_{DP0}^2 + 8Q_{DP0}^3)}{120Q_{eff}^2} \\ & - \frac{Q_{eff} (Q_{DPL} - Q_{DP0})^2 (45Q_{DPL}^2 + 50Q_{DPL} Q_{DP0} + 25Q_{DP0}^2)}{120QE Q^2} \\ & - \frac{(Q_{DPL} - Q_{DP0})^2 (40Q_{DPL} + 20Q_{DP0})}{120} \end{aligned} \quad (\text{B.51})$$

Solution to integration of Equation (5.75)

$$\begin{aligned}
Q_{dC} = & - \frac{(Q_{CL} - Q_{C0})^2 (6Q_{CL}^3 + 12Q_{CL}^2 Q_{C0} + 8Q_{CL} Q_{C0}^2 + 4Q_{C0}^3)}{60C_C^2 \eta^2 \phi_t^2} \\
& - \frac{\eta (Q_{CL} - Q_{C0})^2 (45C_C \phi_t Q_{CL}^2 + 50C_C \phi_t Q_{CL} Q_{C0} + 25C_C \phi_t Q_{C0}^2)}{60C_C^2 \eta^2 \phi_t^2} \\
& - \frac{(Q_{CL} - Q_{C0})^2 (80C_C^2 Q_{CL} \phi_t^2 + 40C_C^2 Q_{C0} \phi_t^2)}{60C_C^2 \phi_t^2}
\end{aligned} \tag{B.52}$$

APPENDIX C

PUBLICATION LIST

C.1 International Journal

1. Afiq Hamzah, N. Ezaila Alias and Razali Ismail, Low-Voltage High-Speed Programming Gate-All-Around Floating Gate (GAA-FG) Memory Cell with Tunnel Barrier Engineering, (2018). Japanese Journal of Applied Physics, 57(6S3), pp. 06KC02-1–06KC02-8 [Q3, IF=1.384].
2. Afiq Hamzah, M. A. Hilman, N. Ezaila Alias and Razali Ismail, “Scaling Challenges of Floating Gate Non-Volatile Memory and Graphene as the Future Flash Memory Device: A Review”, Journal of Nanoelectronics and Optoelectronics, (2018) [Q4, IF=0.45]. (Accepted)
3. Afiq Hamzah, Fatimah A. Hamid, and Razali Ismail. (2016). Explicit Continuous Charge-Based Compact Model for Heavily Doped Surrounding-Gate MOSFETs Incorporating Interface Traps and Fixed Oxide Charges. Journal of Semiconductor and Science Technology, 31(12), pp. 1–13. [Q2, IF=2.13].

C.2 International Conference Proceeding

1. Afiq Hamzah, Zaharah Johari, and Razali Ismail, “A charge-based compact modeling of cylindrical surrounding-floating gate MOSFET (S-FGMOSFET) for memory cell application,” in IEEE International Conference on Semiconductor Electronics, Proceedings, ICSE, 2016, pp. 157–160.
2. Afiq Hamzah and Razali Ismail, “Performance Prediction of Graphene Nanoribbon and Carbon Nanotube Transistors,” in IEEE International Conference on Semiconductor Electronics, Proceedings, ICSE, 2016, pp. 149–152.

3. Afiq Hamzah, A. Adila Syaidatul, Razali Ismail, and Z. Johari, "Performance Benchmarking of Graphene Nanoscroll Transistor with 22nm MOSFET Model," in Regional Symposium on Micro and Nanoelectronics, 2015, pp. 1–4.